REAL-TIME TORQUE RIPPLE MINIMIZATION OF OUTER ROTOR SWITCHED RELUCTANCE MOTOR

A Thesis

by

YONGQI LI

Submitted to the Office of Graduate and Professional Studies of
Texas A&M University
in partial fulfillment of the requirements for the degree of

MASTER OF SCIENCE

Chair of Committee,	Hamid Toliyat
Committee Members,	Shankar P. Bhattacharyya
	Prasad Enjeti
	Yong-Joe Kim
Head of Department,	Miroslav M. Begovic

May 2016

Major Subject: Electrical Engineering

ABSTRACT

The Switched Reluctance Motor (SRM) is becoming more and more attractive because of its simple structure, robustness and cost-efficiency. It is a good candidate for variable speed applications such as Electric Vehicles (EVs), electric ships, aerospace, wind turbines, etc. However, the SRM inherently suffers from high torque ripple which is the main limitation preventing its use in high-performance applications. To reduce this torque ripple, the turn-on and turn-off angles of the motor phases can be adjusted.

In this thesis, the SRM fundamentals are investigated along with the inductance model. For the linear case, the inductance is calculated using the analytical method. The non-linear model is then discussed as an improvement to this method. Control loops are designed based on the system block diagrams which are derived from the small signal model. The turn-on angle is calculated according to the operating conditions, and the turn-off angle is varied within a small range. At each combination of turn-on and turn-off angles, torque ripple, which is defined as the summation of the differences between each instantaneous torque and the average torque, is estimated and compared with other combinations. Based on these results, the best firing angle is selected to achieve the minimum possible torque ripple. The method is verified using simulations in Matlab/Simulink and physical experiments. The control algorithm is implemented on a microcontroller for the experiments and it is able to tune the firing angles in real time at different operating conditions. Spectrum analysis of the torque signal is used to prove the reduction of torque ripple.

To my parents

ACKNOWLEDGEMENTS

First of all, I would like to give the sincerest thanks to my advisor Dr. Hamid Toliyat, for all of the instructions, encouragements and support he gave to me. His solid knowledge, enthusiasm towards research, care of each student deeply impress me and make me feel extremely honored to be able to study with him. The time working under his instruction is the lifelong invaluable experience for me. He always owns my genuine respect and gratitude.

I'm grateful to my committee members, Dr. Shankar Bhattacharyya, Dr. Prasad Enjeti and Dr. Yong-Joe Kim for spending their valuable time reviewing my thesis and attending my defense. Moreover, I thank them for their courses which provided me important trainings.

I also want to express thanks to my co-worker, Miss Bahar Anvari. She introduced me into this project and provided help in all aspects during the course of research. She is an outstanding teammate – smart, easy to communicate, willing to share, genuine to people. Her help and encouragement mean a lot to me. It is always a pleasure to collaborate with her.

In addition, I want to thank Dr. Jae-Bum Park for his suggestions and his circuit board which is an important part of the experiment setup. I thank Dr. Yateendra Deshpande for helping with the testbed design, programming of DSP and so on. He is brilliant and always willing to provide useful suggestions. I would like to thank Dr. Vivek Sundaram for his help in many detailed problems and sharing his knowledge and experience selflessly, with every person in need of his suggestions. My thanks also goes to Morteza Moosavi, who offers help without hesitation every time I asked him. Also I want to thank Matthew Johnson for his testbed advice and many assistances in laboratory issues. He devotes his time to organizing the lab and making others' life easier. Besides, thanks all the other EMPE lab colleagues, Abdulkadir Bostanci, Matthew Gardner, Hussain Hussain, Khaled Ali Al Jaafari, Ajay Morya, Amir Negahdari, Niloofar Torabi and Arash Torkan, who help make my time in the lab comfortable and meaningful in the lab.

Besides, I thank all my friends with whom my life here is enjoyable.

Finally, I thank my parents for all the care, concern, love and encouragement. They are the people who I can always rely on; they are the people who love and care me most. Without their support, I was not able to finish my degree here.

NOMENCLATURE

B	Coefficient of friction torque
g	Air gap thickness
J	Motor inertia
l_e	Motor stack length
$L(\theta, i)$	Phase inductance, function of rotor angle and current
m	Number of phases
N_r	Number of rotor poles
N_s	Number of stator poles
R_s	Phase resistance
S	Number of strokes per revolution
T_e	Electromagnetic torque
T_l	Load torque
T_m	Mechanical time constant
V_{dc}	DC bus voltage
W_c	Co-energy
W_e	Electrical energy input
W_f	Magnetic stored energy
W_m	Mechanical energy output
β_r	Rotor pole arc
β_s	Stator pole arc

θ	Rotor position
θ_a	Aligned position
θ_u	Unaligned position
θ_{off}	Turn-off angle
θ_{on}	Turn-on angle
θ_{sk}	Stroke angle
τ_r	Rotor pole pitch
τ_s	Stator pole pitch
ω	Motor speed

TABLE OF CONTENTS

Page

LIST OF FIGURES

Page

Page

LIST OF TABLES

Page

1 INTRODUCTION

1.1 Background

Over the past several decades the Switched Reluctance Motor (SRM) has grown in popularity and received significant research interest in various studies [1-3]. These studies can be generally categorized into several areas, such as inductance and flux linkage measurements [4-7], mathematical models of SRM focusing on the inductance and torque [8, 9], motor design and optimization [10-12], and drive and control [13-17]. SRMs offer the advantages of simple structure, cost-effectiveness, and robustness [18, 19]. Because SRMs only have windings on the stator and no windings or magnets on the rotor, this eliminates the threats of rotor winding failure, magnet retention issues, and demagnetization, making the machines very reliable even in harsh environments [20]. In addition, because SRMs do not require magnets their price is not influenced by rare earth magnet materials which makes them a cost-effective candidate for many applications.

Energy conversion in SRMs is closely related with power electronics devices. Each phase of the SRM is controlled independently and the identical converter topology can be utilized for every phase. Several topologies are introduced and compared in [17]. Due to the simple structure without rotor magnets or windings, there are no conventional north and south poles on the stator. As a result, the stator excitation current is unidirectional. This not only simplifies the converter control, but also provides more possibilities for topologies to minimize the requisite number of switches.

Despite all of the aforementioned advantages, SRMs do suffer from high torque ripple, which is a significant disadvantage. This is a result of the phase commutation and can be mitigated through the use of motor design and control techniques. Since the transition period is decided by the turn-on angle θ_{on} and turn-off angle θ_{off} of the phases (also referred as firing angles), good control with small torque ripple requires proper turn-on and turn-off angles for smooth transitions. The details of determining firing angles will be included in the thesis.

1.2 Applications of SRM

The Switched Reluctance Machine can be used in many variable speed applications. Numerous studies have explored the design and control issues of SRMs for Electric Vehicle (EV) and Hybrid Electric Vehicle (HEV) [19, 21, 22]. Additionally, some research has been done for winding turbine applications [23-25]. Other kinds of applications such as mining, hard disk drive, home appliances, aerospace, etc. were also investigated in the past.

The SRM studied in this thesis has an outer rotor structure and is designed for hub-mounted in wheel electric vehicle applications. Vehicle operation consists of three main segments: initial acceleration, cruising at the rated speed, and cruising at the maximum speed. These three operation regions provide the basic design constrains for EV/HEV. The motor must be able to meet these constrains so that it can also function properly in other operational regions.

1.3 Objectives and Thesis Overview

The purpose of this thesis is to implement the digital control of an SRM using a microcontroller and to reduce the machine's torque ripple through optimization of the firing angles. The control algorithm should be able to estimate the electromagnetic torque and tune the firing angles in real time. The thesis analyzes the motor inductance and torque characteristics based on Finite Element Analysis (FEA) and the mathematical model is discussed. The speed and current control loops are designed then applied in both simulations and experiments. Torque ripple and firing angles are studied in simulation/experiments to find the best turn-on and turn-off angles under different operating conditions.

The thesis is organized as follows:

The second section introduces the fundamentals of SRMs in general, including motor structure, working principals, inductance measurement method, energy conversion, converter topology and control strategies. The discussion in this section is not focused on a specific motor.

The third section starts with specifications of the Switched Reluctance Motor used in the thesis. The phase inductance at the unsaturated condition is then calculated using an analytical method. This is followed by a study of the non-linear inductance model and the resulting torque calculation. Comparison between the inductance model and FEA is presented to show the accuracy of the model.

The fourth section deals with control of the motor. The transfer function of each part is derived and the system block diagrams are developed. Both the inner current loop and outer speed loop utilize a PI controller. These two control loops are designed and verified with respect to the stability and transient response performance.

The fifth section explains the Matlab/Simulink simulations and the experimental verification. The Simulink model mainly consists of power converters, the SRM model, switch signals and position sensor feedback. For torque ripple reduction, θ_{on} is determined according to the speed and operating current; then θ_{off} is varied within a small range to find the best turn-off angle for reducing the torque ripple. The Matlab script is used to automatically calculate θ_{on} and vary θ_{off}. In order to experimentally verify the simulation results, a testbed for this outer rotor structure was first designed in SolidWorks and then machined. The Texas Instruments (TI) Digital Signal Processor (DSP) TMS320F28335 is used to control the motor. An interface board is connected between DSP and power converters to handle PWM signals and sense phase currents. Position information is fed into the DSP by an encoder mounted on the shaft. The code is capable of tuning θ_{on} and θ_{off} at any speed and load torque, in order to find the best firing angles for torque ripple minimization.

The last section summarizes the work done in this thesis.

2 FUNDAMENTALS OF SWITCHED RELUCTANCE MOTOR

2.1 Structure and Working Principles

The SRM has a doubly salient structure and only stator phases have windings which is the most notable feature of its simple structure. The stator windings are concentric coils on each pole. The motor can be either conventional inner rotor or outer rotor, as shown in Fig. 2.1 and Fig. 2.2. Fig. 2.1 shows a four-phase inner rotor SRM with 8 stator poles and 6 rotor poles which is a very common design configuration. Fig. 2.2 shows the outer rotor SRM studied in this thesis, which has 4 phases 16 stator poles and 20 rotor poles. Only phase A windings are drawn in the figure. Assume the positive signs represent north poles and the negative signs represent south poles.

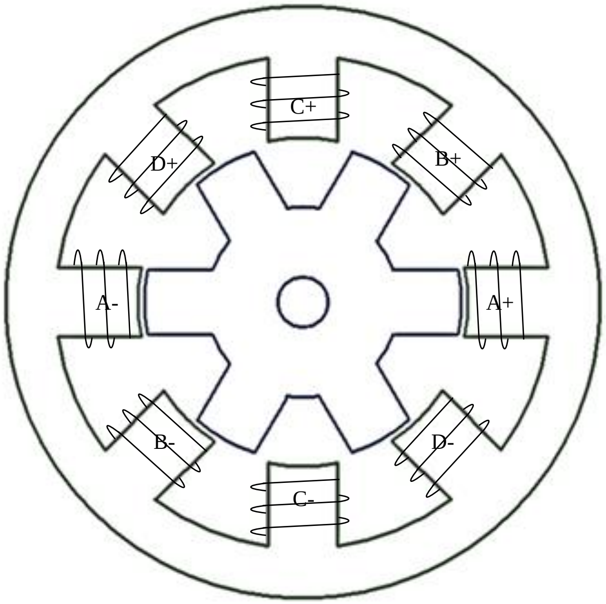

Fig. 2.1 An inner rotor SRM example

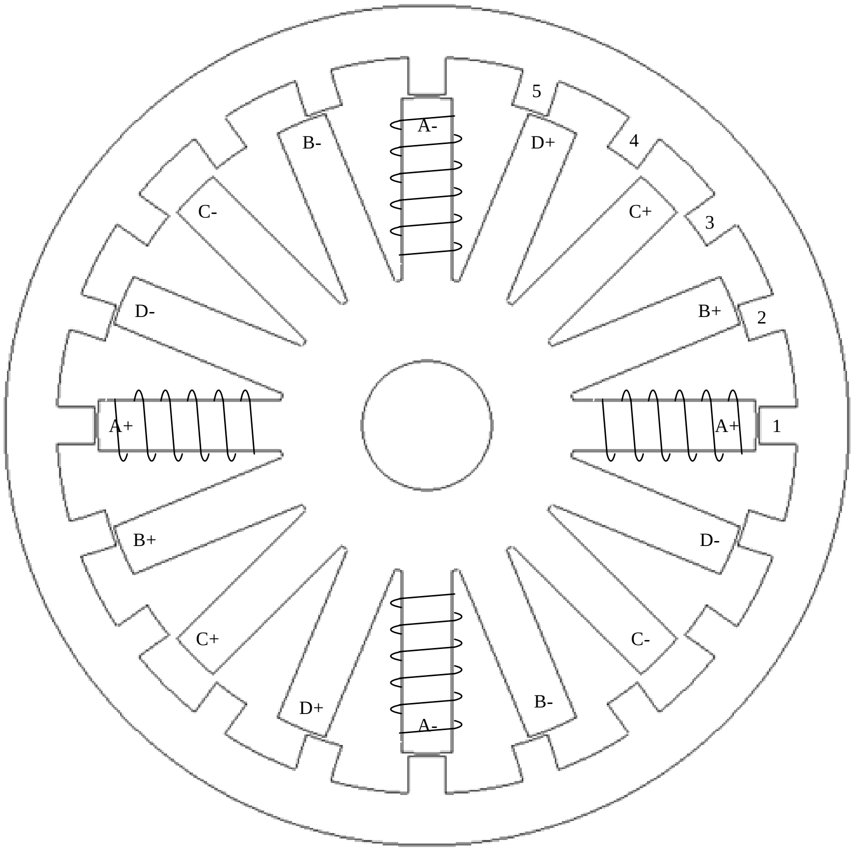

Fig. 2.2 The SRM studied in this thesis

The operation of a Switched Reluctance Motor is based on the minimal reluctance path principle, which means the rotor always tends to move to the position at which the reluctance path is minimized. There are two important positions: the aligned position θ_a and the unaligned position θ_u. The aligned position corresponds to the center of the stator and rotor poles facing each other, while the unaligned position indicates that the center of the stator pole coincides with the center of the rotor interpolar gap. As shown in Fig. 2.2, phase A is aligned and phase C is unaligned.

The flux path reluctance is given by

$$R = \frac{l}{\mu A} \tag{2.1}$$

where *R* is reluctance, *l* is flux path length, μ is permeability and *A* is cross section area of flux path. The relation between reluctance and inductance is

$$L = \frac{N^2}{R} \tag{2.2}$$

It can be seen that the reluctance is proportional to path length and the inductance is inversely proportional to path length. When the motor is at the aligned position the inductance is maximized while at the unaligned position the inductance is minimized. Thus the motor inductance is a function of position. Fig. 2.3 shows the idealized inductance and current profiles. If current is applied during the interval when the inductance is increasing, meaning the rotor is moving toward the aligned position, torque will be produced and the switched reluctance machine will work as a motor. On the contrary, if current is applied when inductance is decreasing, the machine will work as a generator.

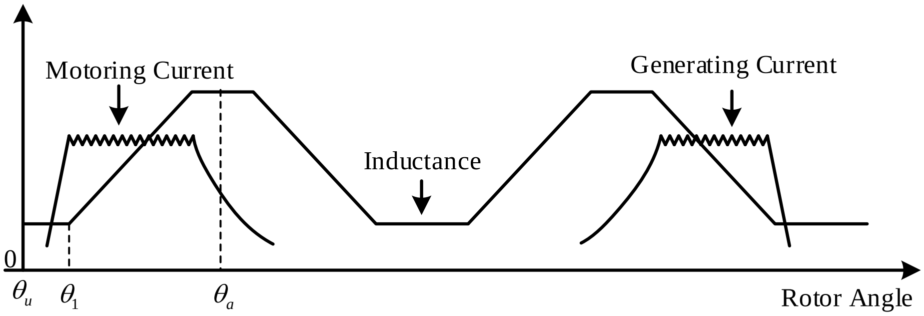

Fig. 2.3 Idealized inductance and current profiles [23]

Energizing the stator phases sequentially causes the rotor poles to repeatedly align with the nearest energized stator pole and forces the motor to rotate. Take the motor in Fig. 2.2 as an example. Phase A is energized first and rotor pole 1 aligns with pole A+. Next energize phase B and pole 2 will align with pole B+. Finally phase A is energized again and pole 5 will align with pole A-. Thus, during one electrical cycle the rotor rotates one rotor pitch, β_{rp}. This analysis demonstrates that a rotation of one rotor pitch requires 4 strokes or 4 phase commutations. To rotate one revolution, it requires Nr electrical cycles. In general, the stroke angle can be defined as:

$$\theta_{sk} = \frac{360°}{m \cdot N_r} \tag{2.3}$$

and the number of strokes per revolution is:

$$S = m \cdot N_r \tag{2.4}$$

It should be pointed out that the north and south polarity of each stator pole does not change (the magnetic flux direction of a certain pole does not change) unlike in induction or PM motors. Thus the phase current is always unidirectional in SRMs.

2.2 Comparison

2.2.1 Synchronous Reluctance Motor

As suggested by the resemblance between names, it is logical to compare SRMs with synchronous reluctance motors (SynRMs). Since SynRMs do not have rotor windings or magnets they also have the same aforementioned advantages of SRM. SynRMs have equal number of stator and rotor poles. The projections on the rotor are arranged to introduce internal flux “barriers”, holes which direct the magnetic flux along the polar axis (d-axis). The following Table 2.1 compares switched reluctance motors and synchronous reluctance motors [2].

Table 2.1 Comparison of SRM and SynRM

SRM	SynRM
1. Double salient poles	1. Smooth surface on both stator and rotor
2. Each stator winding is wound on one pole	2. Multiphase winding with sine distribution
3. Sequential current pulses excitation to each phase	3. Sinusoidal excitation
4. Triangular or sawtooth flux waveform	4. Sinusoidal self-inductance waveform

2.2.2 Stepper Motor

Stepper motors experiences similarity to SRMs with respect to their topology and working strategy. However the machines also have important differences in design, control algorithm, performance and application. In particular, a stepper motor is usually run open loop and designed to maintain step accuracy in position controls.

2.3 Selection of Phase and Pole Numbers

The numbers of stator phase and motor poles are important design parameters. Proper configurations can increase torque density, smooth the phase transition process and reduce torque ripple.

2.3.1 Number of Phases

To determine the number of phases, the following factors can be considered [1].

1. Cost - Since stator phases are controlled independently, each phase requires a set of hardware, including a power converter, drive, current sensor, etc. As a result, increasing the number of phases will increase the system cost.
2. Reliability - A higher number of phase can increase fault tolerance capabilities. When one or more phases fail, the motor can still operate without additional special control.
3. Power density - Power density tends to increase with the number of phases.
4. Efficiency - As the number of phases increases, the switching frequency also has to increase which leads to higher core and switching losses. As a result the efficiency is reduced.

Other factors such as starting capability and directional capability can also be taken into consideration. At the meantime, the number of stator and rotor poles affect these factors together with the phase number.

2.3.2 Number of Stator and Rotor Pole

Some of the common combinations of stator and rotor poles are listed in the following Table 2.2 [2]. From the table, it can be concluded that stator and rotor poles are always even numbers and the ratio of stator pole over rotor pole is usually a non-integer. For the common combinations listed in the table, the pole number relation can be represented by

$$N_r = N_s \pm 2 \cdot \frac{N_s}{2m} \tag{2.5}$$

It should be noted that there are other available combinations which do not agree with this equation.

Table 2.2 Common combinations of stator and rotor pole numbers

m	N_s	N_r	θ_{sk}	S
2	4	2	90°	4
	8	4	45°	8
3	6	4	30°	12
	6	8	15°	24
	12	8	15°	24
4	8	6	15°	24
5	10	8	9°	40
6	12	10	6°	60

After choosing the pole numbers, stator and rotor pole pitches (β_{sp} and β_{rp}) can be determined. But the ratio of pole arc to pole pitch is still a design variable. This ratio can be defined as pole enclosure. [26] discusses the effect of stator and rotor pole enclosures on average torque. By analyzing different combinations of pole enclosures and current levels, it is concluded that the stator pole enclosure should be in the range of 0.35 to 0.5 and the rotor pole enclosure in the range of 0.3 to 0.45.

2.4 Inductance Measurement

The SRM equivalent circuit is shown in Fig. 2.4 as a series *R*-*L* circuit. Although this circuit seems simple, it is severely complicated by the fact that the inductance is a function of both rotor position and stator phase current. When the motor is saturated, current influence comes into the picture and the inductance becomes non-linear.

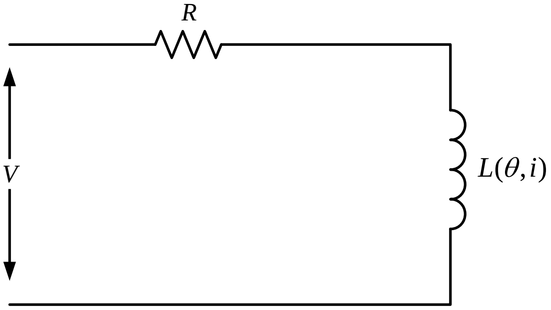

Fig. 2.4 Equivalent circuit of one phase

The phase equation can be expressed as (2.6) and further expanded to (2.7).

$$v = R_s i + \frac{d\lambda}{dt} \tag{2.6}$$

$$\begin{aligned} v &= R_s i + \frac{d(L(\theta,i)\cdot i)}{d\theta} \\ &= R_s i + L(\theta,i)\frac{di}{dt} + i\frac{dL(\theta,i)}{d\theta}\frac{d\theta}{dt} + i\frac{\big(dL(\theta,i)\big)}{di}\frac{di}{dt} \\ &= R_s i + L(\theta,i)\frac{di}{dt} + i\omega\frac{dL(\theta,i)}{d\theta} + i\frac{\big(dL(\theta,i)\big)}{di}\frac{di}{dt} \end{aligned} \tag{2.7}$$

where v is the phase voltage and i is the current. If the inductance variation's dependence on current is neglected, the last term in (2.7) is eliminated and it reduces to the more common form given in (2.8).

$$v = R_s i + L(\theta,i)\frac{di}{dt} + i\omega\frac{dL(\theta,i)}{d\theta} \tag{2.8}$$

This is a reasonable approximation because in the control scheme, current is regulated to an almost constant value so the inductance variation caused by current can be ignored.

As a very important parameter, the inductance and its measurement always receive a significant amount of attention. If the actual inductance profile is known, then one can better analyze the motor performance and predict the torque produced. This is very important in direct torque control. Reference [6] investigated several measurement methods and they are summarized below.

1. Utilizing the *R-L* circuit response to a step input, applying a DC voltage to the motor phase and measuring the transient current response during the energizing period. Based on (2.6), voltage and current can be integrated from the initial state to steady state so that flux linkage can be calculated. Dividing the flux by the steady state current gives the inductance. The integration process can easily be done by using some advanced oscilloscopes.
2. Applying an AC voltage to the phase then measuring the voltage and current. Impedance can be calculated from the RMS values. This impedance and knowledge of the phase resistance can be used to calculate the inductance. If phase resistance cannot be accurately determined, then the phase shift between the current and voltage waveforms together with the impedance may be used to calculate the inductance.
3. There is also a DC+AC method, in which a small AC voltage is imposed on the DC voltage. The magnetic circuit operating point is set by the DC voltage, while the AC voltage introduces sinusoidal current which works similarly to the second method. The advantage of this method is that current will not be distorted too much by saturation, compared to the pure AC method, so that it gives more accurate results at high current levels.
4. Measurements with a search coil.

2.5 Energy Conversion

The Switched Reluctance Motor is an electromechanical energy conversion device that converts the input electrical energy to mechanical energy. During the conversion, part of the input energy is stored in the magnetic field. Fig. 2.5 shows the definition of stored field energy and co-energy. Their mathematical expressions are given by

$$W_f = \int_0^{\lambda_0} i(\lambda)\, d\lambda \tag{2.9}$$

$$W_c = \int_0^{i_0} \lambda(i)\, di \tag{2.10}$$

In Fig. 2.6, AB represents a position displacement $\Delta\theta$. When moving from A to B, the input energy change is

$$\Delta W_e = \int ei\, dt = \int i\, d\lambda = ABCD \tag{2.11}$$

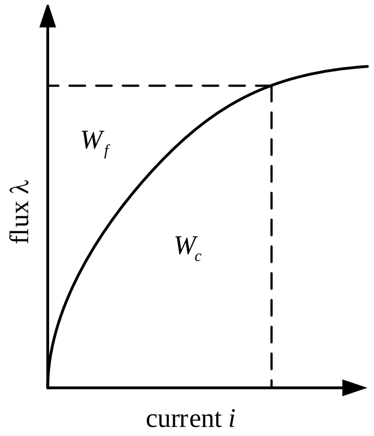

Fig. 2.5 Definition of stored magnetic energy and co-energy [2]

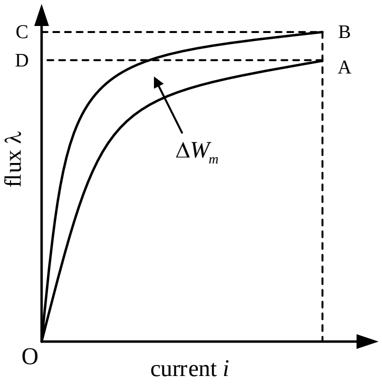

Fig. 2.6 Energy conversion [2]

The mechanical energy ΔW_m is the area of OAB and is equal to the co-energy change in this case. Torque can be calculated by

$$T = \frac{\partial W_c}{\partial \theta} = \frac{\partial}{\partial \theta} \int_0^{i_0} [L(\theta, i) \cdot i] \, di \tag{2.12}$$

When the motor is not saturated, the $\lambda - i$ relation is a straight line, so energy and co-energy are always equal. The torque equation reduces to

$$T = \frac{d}{d\theta} \int_0^{i_0} L(\theta) \cdot i \, di = \frac{1}{2} i_0^2 \frac{dL(\theta)}{d\theta} \tag{2.13}$$

which is referred as the linear torque equation since the inductance is not saturated and is independent of current. Correspondingly, (2.12) is the non-linear torque expression.

2.6 Converter Topology and Control Strategy

The most commonly used converter topology is the asymmetric full bridge converter which consists of two switches and two diodes in each phase. This topology allows fully independent control of every individual phase, but unfortunately it also requires a large number of devices. The cost is particularly challenging in multiphase system. Fig. 2.7 shows this topology for one phase and it is identical for the other phases.

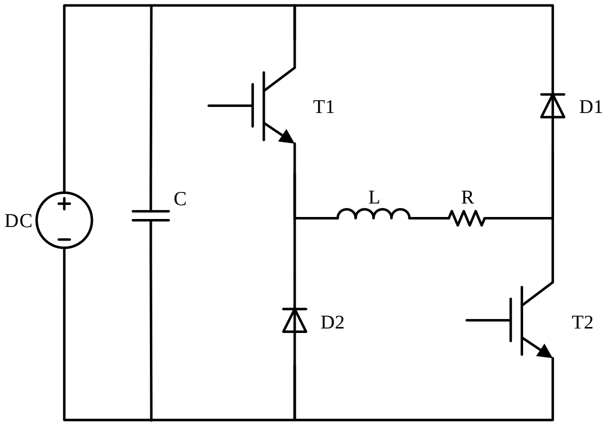

Fig. 2.7 Asymmetric full bridge converter

Two strategies of controlling the phase current are hysteresis control and PWM control. Hysteresis controller has the advantages of simple implementation, fast response and motor independence [17]. However, the switching frequency is variable which leads to larger acoustic noise compared to the fixed frequency PWM controller. Moreover, because of the current sampling rate limitation and the time delay between sampling and switching in any practical digital implementation, the hysteresis controller usually results in higher current ripple. In hysteresis control, current error directly controls switches; whereas in PWM control the error is first processed by a proportional-integral (PI) controller and then the outputs serves as the PWM compare value. This difference makes the hysteresis controller inherently more sensitive to sampling noise and exacerbates the already higher current ripple. Therefore, a PWM controller is utilized in this thesis.

The purpose of the current controller is to regulate the current and force it to follow the reference by turning on and off switches. Regardless of which kind of controller is adopted for the full bridge converter, there are two switching strategies, namely hard chopping and soft chopping [27]. Fig. 2.8 illustrates the different switch statuses. Solid lines represent the current flow paths and the non-conducting paths are shown as dashed lines. At the beginning of phase conduction, both switches, T1 and T2, are on as shown in subfigure (a) and current rises from zero to its reference. Positive voltage is applied to the phase at this stage. When the phase is about to shut off at the last stage, both switches are turned off and the current freewheels through the two diodes, shown in (c). Negative voltages is applied so the phase current quickly drops to zero. Between these two stages, current is chopped. In hard chopping mode, the switch states change between (a) and (c) while in soft chopping mode, the states change between (a) and (b). With soft chopping, switch T2 is always on during the whole phase conduction period. When T1 is off, current can freewheel through switch T2 and diode D2. During this interval, the voltage on the phase is almost zero.

During the second stage, it is usually desirable for the current to be smooth with a flat-top shape, like in Fig. 2.3. When current is freewheeling in soft chopping mode, zero voltage is applied so the current drops slower than it does during hard chopping. This results in a smaller current ripple at a given switching frequency. Thus in this thesis, the soft chopping strategy is employed.

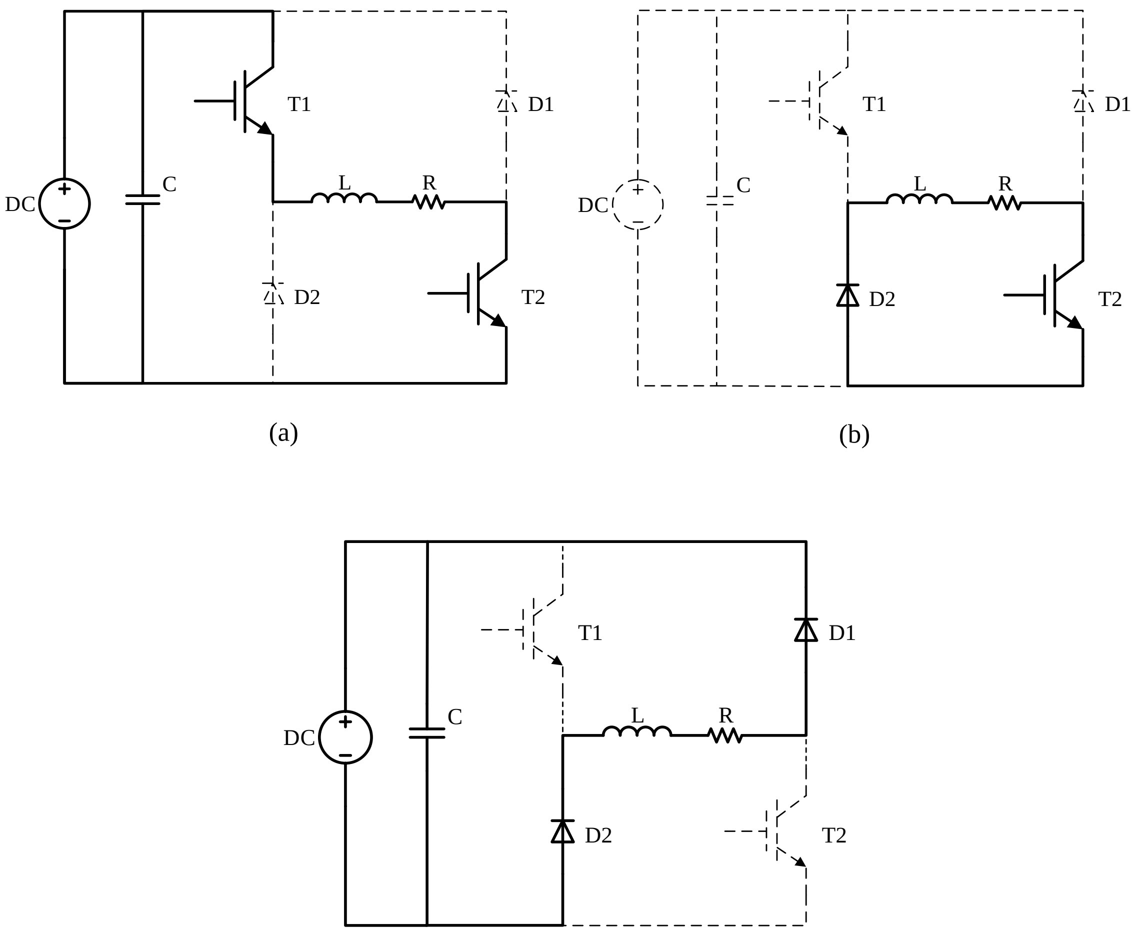

(a) (b)

(c)

Fig. 2.8 Switching strategy

Besides the aforementioned basic operating conditions, there is another condition, called single pulse mode, which can occur due to the current losses control [28]. In this condition, positive voltage is always applied to the phase, but current may still not be able to reach the reference. Thus current is not chopped and regulated. There are several factors which can collectively lead to this operating condition. The third term containing speed and current in (2.8) is referred to the back-EMF. When the motor is running at high speed, the back-EMF may be bigger than the supply voltage and then the current cannot increase anymore. In addition, when moving from the unaligned position to the aligned position, the inductance value increases. This will increase the second term in (2.8) and make the right hand side of the equation greater than the supply voltage. Also at high speed, the rotor passes the interval with a positive inductance slope very quickly and current does not have enough time to build up. The following Fig. 2.9 illustrates this condition.

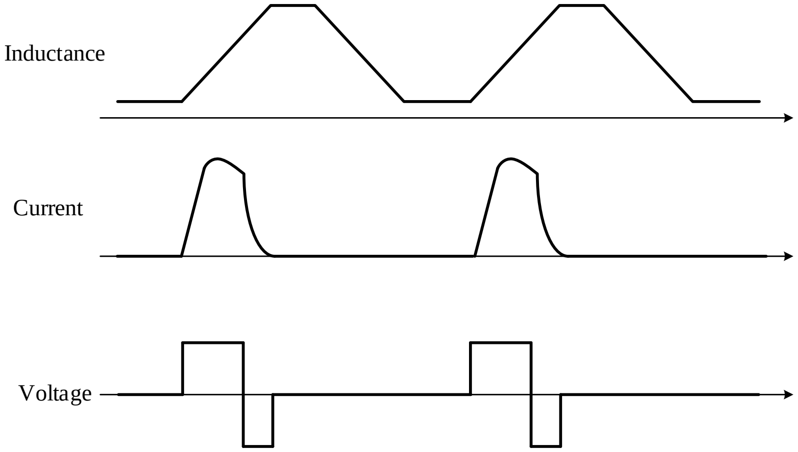

Fig. 2.9 Single pulse mode operation [28]

3 INDUCTANCE MODEL

Several inductance measurement methods were introduced with the last section. After inductance is measured, the information can be developed into a look-up table and stored in the microcontroller for the purpose of control and parameter estimation. But a look-up table may occupy too much memory space so this method is limited by the hardware. The other option is to establish a mathematical model of the inductance. As expected, the inductance model is based on the current and rotor position. Fig. 3.1 and Fig. 3.2 show the inductance profile in 2D and 3D plots, to provide an idea what the inductance should be like for this motor. In the left graph of Fig. 3.1, each line represents different current values and from top to bottom current is decreasing. Similarly, in the right graph different lines represent different positions, varying from θ_a at the top to θ_u at the bottom.

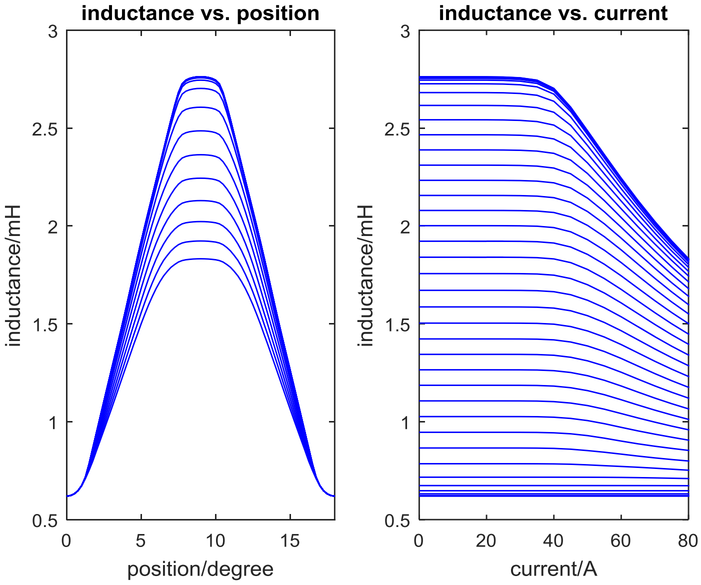

Fig. 3.1 Inductance profile vs. position and current

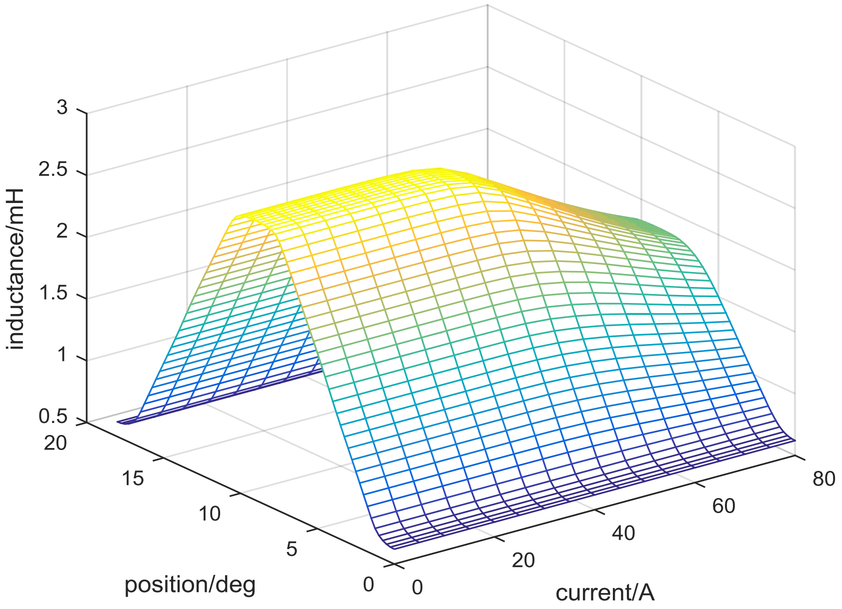

Fig. 3.2 Inductance profile 3D plot

3.1 Motor Specifications

Some electrical and mechanical specifications are listed in Table 3.1 and Table 3.2. The inductance profile is highly dependent on the motor dimensions.

Table 3.1 Electrical specifications for nominal condition

Voltage	60 V
Current	80 A
Speed	560 rpm
Output power	3.75 kW

Table 3.2 Motor mechanical specifications

Stator outer diameter	179.2 mm	Rotor outer diameter	228 mm
Stator inner diameter	35 mm	Rotor inner diameter	180 mm
Stator back iron thickness	25.5 mm	Rotor back iron thickness	14 mm
Stator pole number	16	Rotor pole number	20
Stator pole pitch	22.5°	Rotor pole pitch	18°
Stator pole arc	9°	Rotor pole arc	6.38°

3.2 Analytical Method for Inductance Computation

In this part, the inductance profile under the unsaturated condition is derived using the analytical method. Since the motor geometry is highly symmetric, only one rotor pole pitch is analyzed and the rest is periodic. With this method, given the motor dimension, inductance can be expressed in a closed form in terms of rotor position. The current does not come into effect because only the unsaturated condition is discussed. When the motor is not saturated, the iron reluctance is negligibly small compared to the air gap reluctance. This method can be extended to the saturated condition, but it becomes much more complicated because the iron reluctance becomes non-negligible and it is a function of the current. More details can be found in [1].

Fig. 3.3 and Fig. 3.4 show the flux lines at the aligned and unaligned position respectively, with only one phase energized at 20 Amps which will not saturate the motor. By looking at the flux lines in these two figures, the following primary flux paths are evident.

1. From the top surface of stator tooth to the top surface of rotor tooth;

2. From the top surface of stator tooth to the side surface of rotor tooth;
3. From the side surface of stator tooth to the top surface of rotor tooth;
4. From the top surface of stator tooth to the rotor back iron through rotor slots;
5. From the side surface of stator tooth to the adjacent stator tooth.

Among the above 5 paths, 1-4 correspond to the magnetizing inductance or linkage inductance and 5 corresponds to the leakage inductance. They make up the phase self-inductance. The linkage inductance value varies with position while leakage inductance is considered constant.

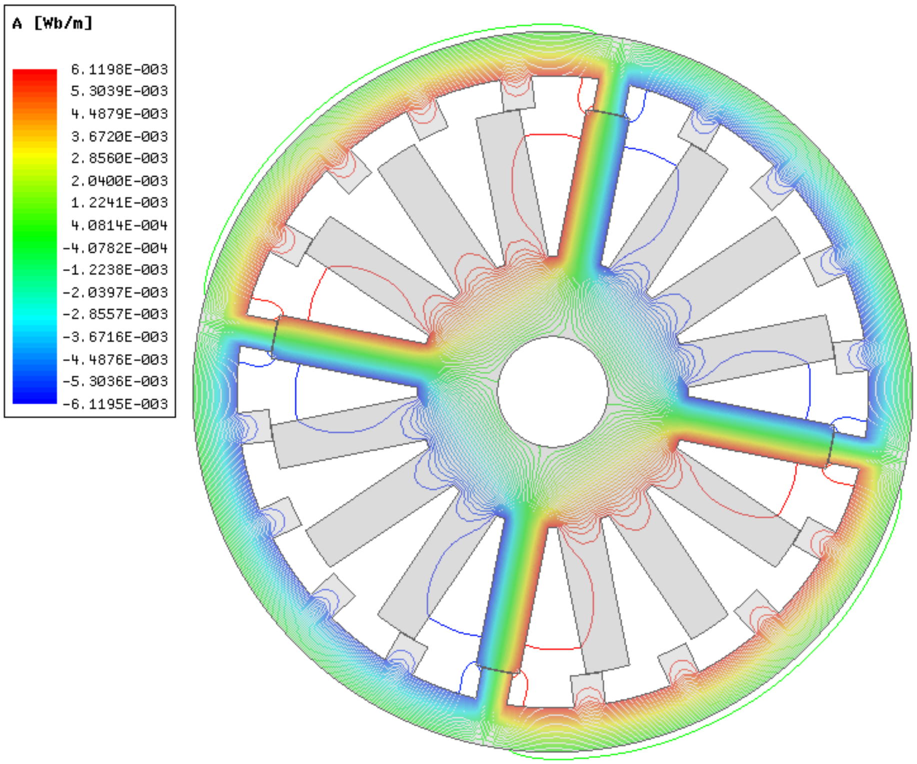

Fig. 3.3 Flux lines at aligned position

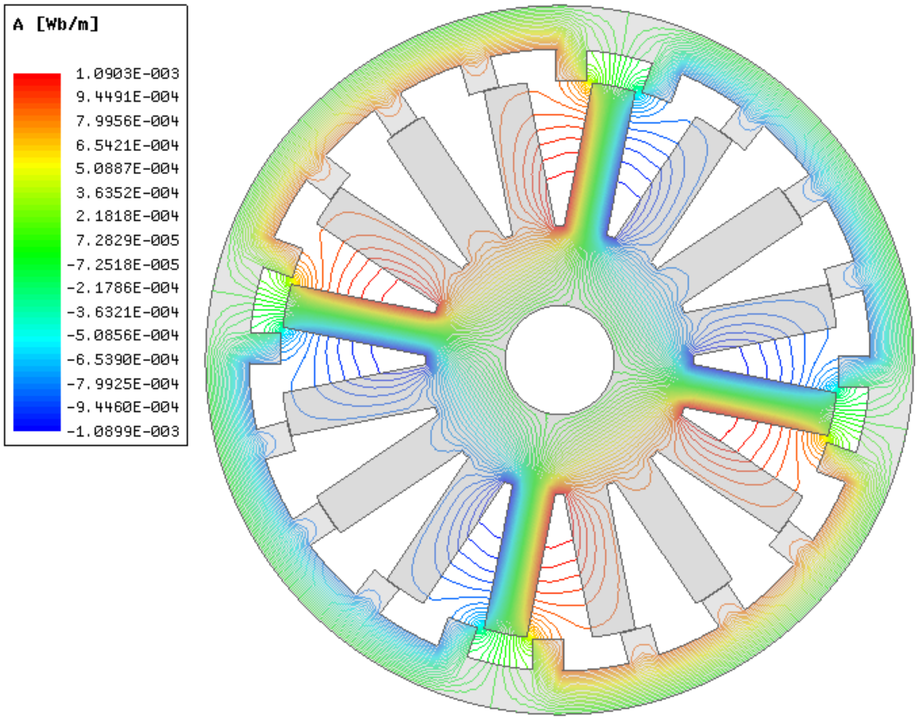

Fig. 3.4 Flux lines at unaligned position

The detailed flux paths of one stator/rotor pole are shown in Fig. 3.5 and Fig. 3.6. The numbers in the pictures indicates the flux path categories mentioned above. Paths 2 and 3 consist of two straight segments and one quarter circle. The length of one straight segment is equal to the vertical distance between the top surfaces of the stator and rotor teeth; the other straight segment is equal to the horizontal distance between the side surfaces of the stator and rotor teeth. In Fig. 3.6, it is essential to determine d_1 and d_2, which serve as the boundaries between flux paths 2 and 4.

The distinguishing criterion between path 2 and 4 is that whenever path 4 is shorter than path 2, flux should enter from the back iron. The length of path 4 is the rotor slot depth d_{sr} whose value is 10 mm and since the air gap is much smaller, it is neglected. Thus the boundary condition can be described as

$$d_{sr} = \frac{2\pi \cdot d_1}{4} \tag{3.1}$$

where d_1 is the radius of the arc. The relation between distance d_1 and its corresponding central angle θ_1 is

$$\theta_1 \frac{D_{os} + g}{2} = d_1 \tag{3.2}$$

where D_{os} is the stator outer diameter. Thus θ_1 is determined in radians. The central angle corresponding to distance d_2 is θ_2 and it is given by

$$\theta_2 = \tau_r - \beta_r - 2\theta_1 \tag{3.3}$$

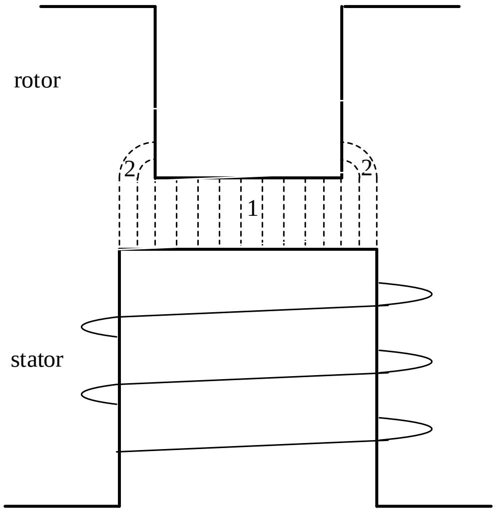

Fig. 3.5 Detailed flux paths at aligned position

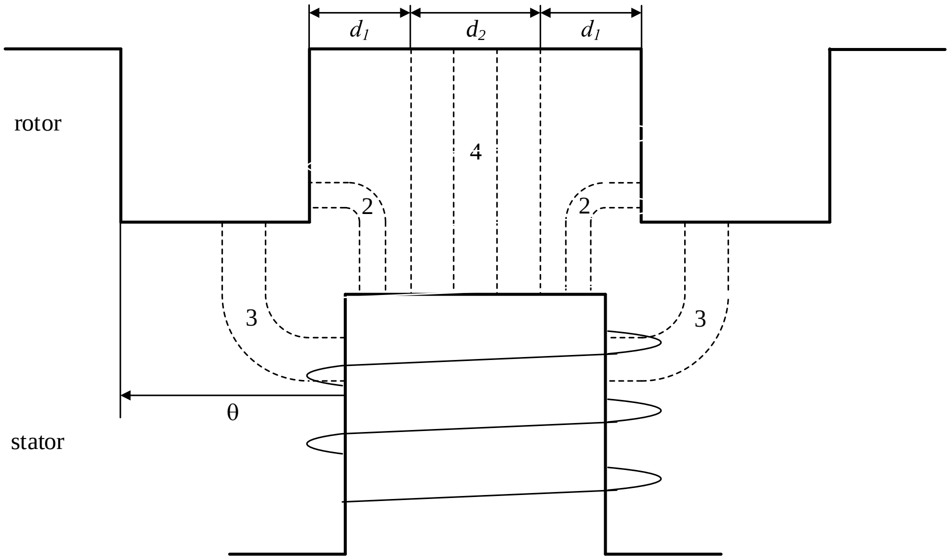

Fig. 3.6 Detailed flux paths at unaligned position

From (2.1) and (2.2), inductance can be calculated as

$$L = \frac{N^2 \mu A}{l} = N^2 P \tag{3.4}$$

in which P is the inverse of reluctance and defined as permeance. The advantage of using permeance instead of reluctance is that when there are several reluctance paths in parallel, the computation of total inductance based on permeance is simply the summation of each part.

Take path 3 when rotor position is between 0 and β_r as an example. For a small section of thickness dr and depth l_e, the permeance is [29]

$$dP = \frac{\mu l_e dr}{g + \frac{\pi r}{2}} \tag{3.5}$$

where dr is calculated by $\frac{D_{os}}{2} d\theta$. So the inductance can be expressed as

$$
\begin{aligned}
L(\theta) &= N^2 \int_0^{\theta_0} \frac{\mu l_e}{g + \frac{\pi r}{2}} dr \\
&= N^2 \frac{2\mu l_e}{\pi} \ln\left(\theta + \frac{4g}{\pi D_{os}}\right)\Bigg|_0^{\theta_0}
\end{aligned}
\tag{3.6}
$$

where θ_0 is between 0 and β_r here. It should be pointed out that at each position, there are several flux paths and they are summed up to get the total inductance expression. Within one rotor pole pitch, several segments have to be divided to find the inductance expression in each segment and at last all segments should be concatenated together. Fig. 3.7 shows the inductance from both the analytical calculation and the Maxwell simulation. The figure demonstrates that there is a very good match between the two results.

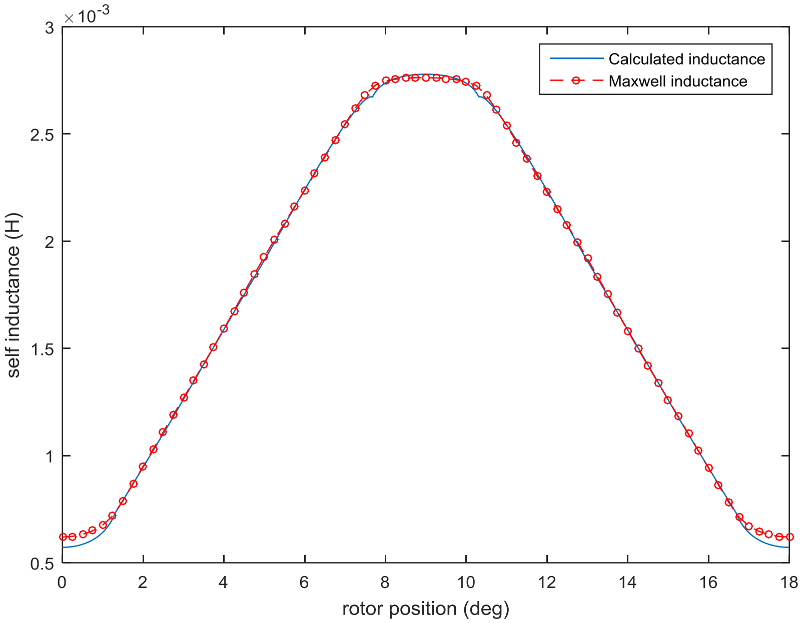

Fig. 3.7 Inductance comparison between analytical method and Maxwell

3.3 Non-linear Model

Although the aforementioned analytical method shows a good estimation of the unsaturated inductance profile, it can become complicated for large currents because then iron reluctance should be included. It is desired to come up with a non-linear inductance model which can express inductance as a function of both current and position [8, 30]. In [9] this model is utilized for sensorless control of SRMs.

The phase self-inductance can be represented by the Fourier Series as

$$L(\theta, i) = L_0(i) - L_1(i)\cos(N_r\theta) + L_2(i)\cos(2N_r\theta) \tag{3.7}$$

where L_0, L_1 and L_2 are functions of current. They can be further represented as

$$L_0(i) = \frac{1}{2}\left[\frac{1}{2}(L_a + L_u) + L_m\right] \tag{3.8}$$

$$L_1(i) = \frac{1}{2}(L_a - L_u) \tag{3.9}$$

$$L_2(i) = \frac{1}{2}\left[\frac{1}{2}(L_a + L_u) - L_m\right] \tag{3.10}$$

where L_a, L_u and L_m are the inductances at the aligned position, the unaligned position and the midway position, respectively. L_a and L_m depend on current, while L_u is almost constant from 0 to the rated current. To develop these expressions, Maxwell FEA simulations are first conducted to obtain inductance profiles at these three positions. Then the data is manipulated to form a quasi-sine waveform so that Fourier Series can be applied. The period is 0-200 Amps which gives a so-called frequency of $2\pi/200$. The expressions are given by

$$L_a(i) = a_0 + \sum_{n=1}^{3} a_n \cos(n\omega i) \tag{3.11}$$

$$L_m(i) = b_0 + \sum_{n=1}^{2} b_n \cos(n\omega i) \tag{3.12}$$

$$L_u = 0.63 \text{ mH} \tag{3.13}$$

where ω is equal to $2\pi/200$. Coefficients are listed in Table 3.3. The inductance is on the order of millihenries. A comparison between this non-linear model and the Maxwell simulation results is depicted in Fig. 3.8.

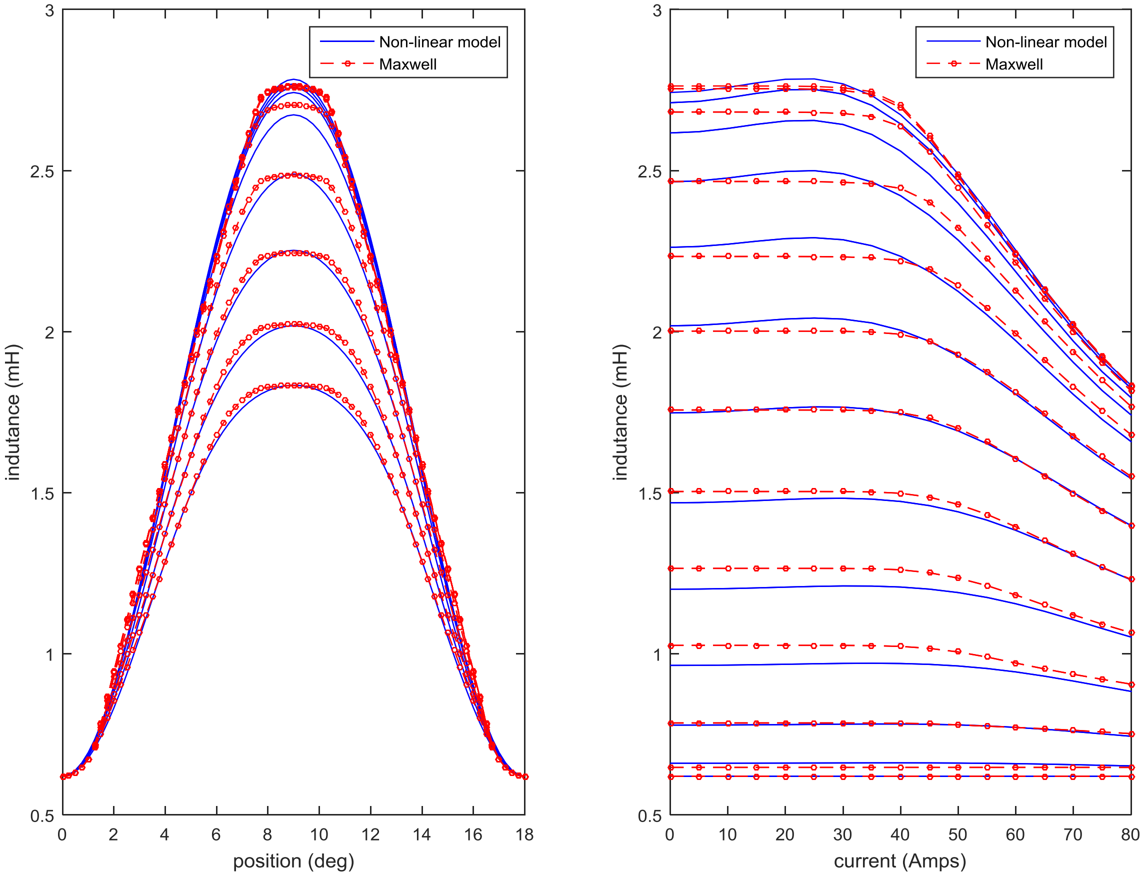

Fig. 3.8 Inductance comparison between non-linear model and Maxwell

Table 3.3 Coefficients for inductance modeling

a_0	2.351	b_0	1.607
a_1	0.571	b_1	0.2255
a_2	-0.138	b_2	-0.0847
a_3	-0.0418		

3.4 Torque Calculation

With the non-linear inductance model, torque is ready to be calculated using (2.12). According to (3.7), the $L_0(i)$ term does not contain position θ so it will not appear in the torque expression. Torque is given by the following equation in the unit of N·m.

$$
\begin{aligned}
T = {} & -\frac{N_r}{4000}\sin(N_r\theta)\Bigg\{L_u i^2 - \Bigg\{a_0 i^2 + 2\sum_{n=1}^{3}\Bigg[a_n\frac{1}{n\omega}\Bigg(i\sin(n\omega i) \\
& + \frac{1}{n\omega}\cos(n\omega i) - \frac{1}{n\omega}\Bigg)\Bigg]\Bigg\}\Bigg\} \\
& - \frac{N_r}{2000}\sin(2N_r\theta)\Bigg\{\frac{1}{2}L_u i^2 + \Bigg\{\frac{1}{2}a_0 i^2 + \sum_{n=1}^{3}\Bigg[a_n\frac{1}{n\omega}\Bigg(i\sin(n\omega i) \\
& + \frac{1}{n\omega}\cos(n\omega i) - \frac{1}{n\omega}\Bigg)\Bigg]\Bigg\} - \Bigg\{b_0 i^2 + 2\sum_{n=1}^{2}\Bigg[b_n\frac{1}{n\omega}\Bigg(i\sin(n\omega i) \\
& + \frac{1}{n\omega}\cos(n\omega i) - \frac{1}{n\omega}\Bigg)\Bigg]\Bigg\}\Bigg\}
\end{aligned}
\qquad (3.14)
$$

4 CONTROL OF SRM DRIVE

A classic dual-loop control is selected for the SRM control scheme, in which the outer loop is responsible for speed control and the inner is responsible for current control. Tuning the gains of the two PI controllers are based on the analysis of transfer functions.

4.1 Derivation of SRM Small Signal Model

Analysis of (2.8) reveals that it involves the multiplication of time-varying quantities, current and position, which leads to a nonlinear system. In order to utilize a vast amount of knowledge on linear system, such as Laplace transformation and frequency domain method, it is advantageous to linearize the system [31]. This can be achieved by constructing a small signal model of which the idea is analyzing the system response to a small input variation at a certain operating point. Besides the voltage equation in (2.8), the torque equation is given by

$$T_e = T_l + B\omega + J\frac{d\omega}{dt} \tag{4.1}$$

With the small signal model, new system states and inputs are

$$i = i_0 + \delta i \tag{4.2}$$

$$\omega = \omega_0 + \delta\omega \tag{4.3}$$

$$v = v_0 + \delta v \tag{4.4}$$

$$T_l = T_l + \delta T_l \tag{4.5}$$

where the subscript 0 indicates steady-state values and the small signals are indicated by δ proceeding the variables. Substituting (2.13) and (4.2)-(4.5) into the system equations

(2.8) and (4.1), to eliminate the steady-state terms and neglecting the second order small signal terms yields:

$$L\frac{d\delta i}{dt} = \left(-R_s - \omega \cdot \frac{dL}{d\theta}\right)\delta i - i_0 \cdot \delta\omega \cdot \frac{dL}{d\theta} + \delta v \tag{4.6}$$

$$J\frac{d\delta\omega}{dt} = i_0 \cdot \delta i \frac{dL}{d\theta} - B \cdot \delta\omega_0 - \delta T_l \tag{4.7}$$

For the sake of simplification, the inductance is assumed to be constant with a value equal to the average of the minimum and maximum inductance at i_0. The derivative term $dL/d\theta$ is the inductance slope at the chosen operating current. In addition, the following substitutions are used:

$$R_e = R_s + \omega_0\frac{dL}{d\theta} \tag{4.8}$$

$$K_b = i_0\frac{dL}{d\theta} \tag{4.9}$$

$$\delta_e = K_b \cdot \delta\omega \tag{4.10}$$

where R_e is the equivalent resistance, K_b is the EMF constant and δ_e is the induced EMF.

The Laplace transformations of (4.6) and (4.7) are given by

$$sL \cdot \delta I(s) = \delta V(s) - R_e \cdot \delta I(s) - K_b \cdot \delta\omega(s) \tag{4.11}$$

$$sJ \cdot \delta\omega(s) = K_b \cdot \delta I(s) - B \cdot \delta\omega(s) - \delta T_l(s) \tag{4.12}$$

Based on the above two equations, the linearized SRM block diagram can be derived as shown in Fig. 4.1. In this block diagram, $\delta I(s)$ is fed back to form a current loop which results in a cross-coupling between the back-EMF and current loop. This complicates the derivation of the transfer function. To simplify the problem, Fig. 4.1 is reconstructed as shown in Fig. 4.2.

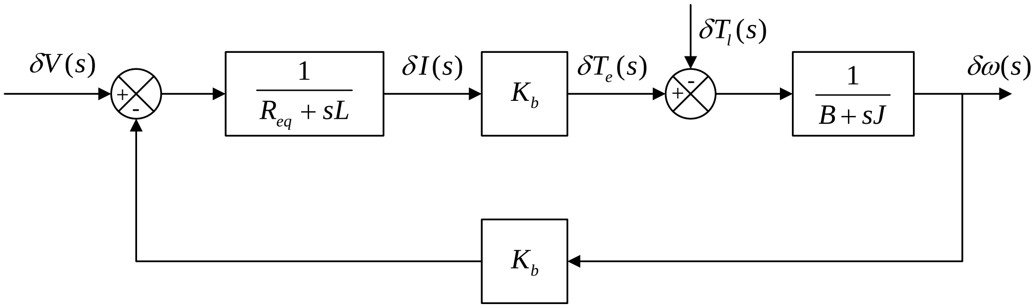

Fig. 4.1 Linearized SRM block diagram [1]

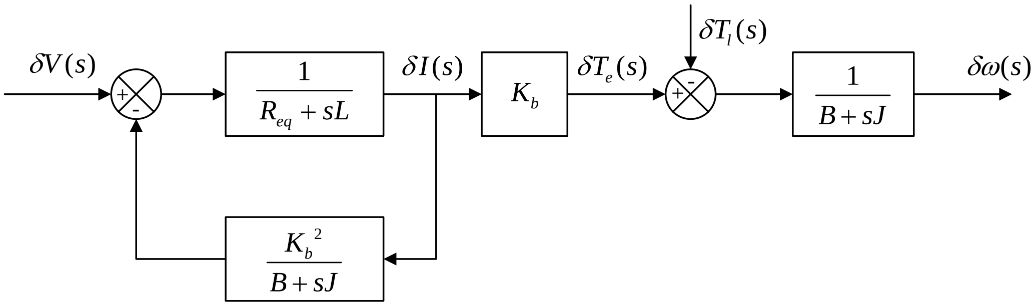

Fig. 4.2 Reconstructed linearized SRM block diagram

From the reconstructed block diagram, it can be determined that

$$\begin{aligned}\frac{\delta I(s)}{\delta V(s)} &= \frac{\dfrac{1}{R_e+sL}}{1+\dfrac{K_b^2}{(R_e+sL)(B+sJ)}}\\ &= \frac{\dfrac{B}{JL}\left(\dfrac{J}{B}s+1\right)}{s^2+\left(\dfrac{B}{J}+\dfrac{R_e}{L}\right)s+\dfrac{R_eB+K_b^2}{LJ}}\\ &= K_1\frac{T_m s+1}{(T_1s+1)(T_2s+1)}\end{aligned} \tag{4.13}$$

where

$$K_1 = \frac{B}{R_e B + K_b^2} \tag{4.14}$$

$$T_m = \frac{J}{B} \tag{4.15}$$

$$-\frac{1}{T_1}, -\frac{1}{T_2} = -\frac{1}{2}\left(\frac{B}{J} + \frac{R_e}{L}\right) \pm \sqrt{\frac{1}{4}\left(\frac{B}{J} + \frac{R_e}{L}\right)^2 - \frac{R_e B + K_b^2}{LJ}} \tag{4.16}$$

So the reduced block diagram of the linearized SRM is obtained as Fig. 4.3 with load torque $\delta T_l(s)$ neglected.

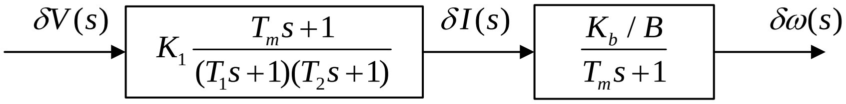

Fig. 4.3 Reduced block diagram of the linearized SRM [1]

Now it can be incorporated into the SRM system block diagram as shown in Fig. 4.4. In the figure, the superscript “*” denotes a reference variable; the subscript “*e*” denotes an error variable.

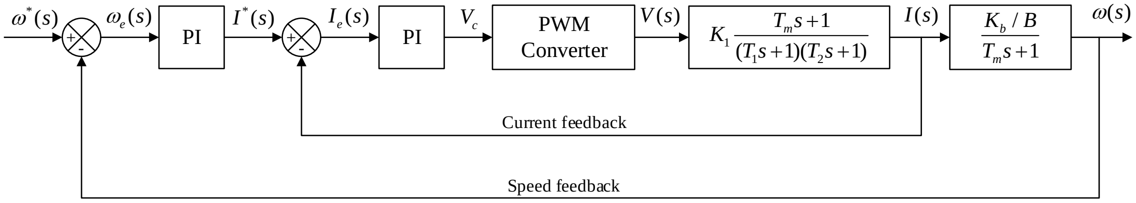

Fig. 4.4 System block diagram

4.2 Design of Current Controller

The current control loop is also shown in Fig. 4.4 as part of the system block diagram. It consists of a PI controller, a PWM converter and the voltage to current transfer function.

The PWM converter can be modeled as a pure delay unit. This is because when the modulation signal of PWM changes, the switch signal does not change immediately. The relation between the control signal duty cycle V_c and the voltage applied on the phase V can be described by

$$\frac{V}{V_c} = V_{dc} \cdot 1(t - T_r) \tag{4.17}$$

where V_{dc} is the DC bus voltage and T_r is the delay between modulation signal change and switch signal change. The maximal delay can be as big as the switching period T_c. In practice, this number can be chosen as half of the switching period, giving

$$T_r = \frac{1}{2f_c} \tag{4.18}$$

in which f_c is the PWM switching frequency. By expanding (4.18) into a Maclaurin Series and given that T_r is relatively small, the expression can be approximated as the following first order lag:

$$\frac{V(s)}{V_c(s)} = \frac{V_{dc}}{1 + T_r s} \tag{4.19}$$

Given that the switching frequency is usually much bigger than the current loop time constant, (4.19) can actually be reduced to the gain value, V_{dc}. Thus the transfer function of the PWM converter is simply V_{dc}.

Since the mechanical time constant is large, $T_m s + 1$ can also be approximated as $T_m s$. The transfer function of a PI controller is usually written as

$$G_c(s) = K_{pc} + \frac{K_{ic}}{s} \tag{4.20}$$

Now the current loop can be drawn as Fig. 4.5.

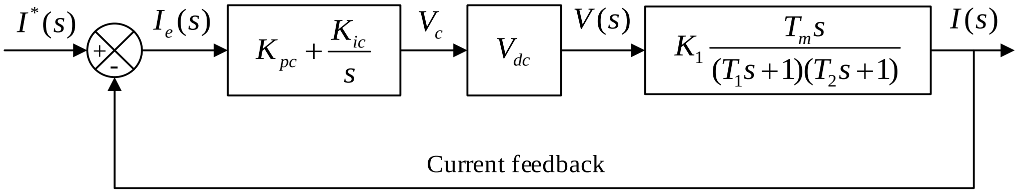

Fig. 4.5 Current loop block diagram

The closed loop transfer function is

$$\begin{aligned} \frac{I(s)}{I^*(s)} &= \frac{(sK_{pc} + K_{ic})V_{dc}K_1T_m}{(T_1s+1)(T_2s+1) + (sK_{pc} + K_{ic})V_{dc}K_1T_m} \\ &= \frac{(sK_{pc} + K_{ic})V_{dc}K_1T_m}{T_1T_2\left(s^2 + \frac{V_{dc}K_{pc}K_1T_m + T_1 + T_2}{T_1T_2}s + \frac{V_{dc}K_{ic}K_1T_m + 1}{T_1T_2}\right)} \end{aligned} \tag{4.21}$$

in which the characteristic equation can be easily recognized as

$$s^2 + \frac{V_{dc}K_{pc}K_1T_m + T_1 + T_2}{T_1T_2}s + \frac{V_{dc}K_{ic}K_1T_m + 1}{T_1T_2} \tag{4.22}$$

Since it is a second order system, the natural frequency ω_n and damping ratios ζ can be used to specify the desired system performance and can further be used to calculate the PI parameters. ω_n and ζ are calculated using the following equations:

$$2\zeta\omega_n = \frac{V_{dc}K_{pc}K_1T_m + T_1 + T_2}{T_1T_2} \tag{4.23}$$

$$\omega_n^2 = \frac{V_{dc}K_{ic}K_1T_m + 1}{T_1T_2} \tag{4.24}$$

Therefore K_{pc} and K_{ic} can be calculated by

$$K_{pc} = \frac{2\zeta\omega_nT_1T_2 - T_1 - T_2}{V_{dc}K_1T_m} \tag{4.25}$$

$$K_{ic} = \frac{\omega_n^2T_1T_2 - 1}{V_{dc}K_1T_m} \tag{4.26}$$

The equivalent time constant for a second order system is $\frac{1}{\zeta\omega_n}$ [32]. If choosing ζ=0.707, then the current loop bandwidth can be roughly estimated as ω_n. So with the choice of ω_n=1500 Hz and other necessary parameters listed in Table 4.1, the calculated results are

$$K_{pc} = 0.262$$

$$K_{ic} = 1820$$

Table 4.1 Parameters used to design the current loop PI controller

i_0	80 A	R_e	0.684 Ω
ω_0	560 rpm	K_b	0.85
V_{dc}	60 V	K_1	1.367×10^{-2}
L	1.23 mH	T_1	0.206
$dL/d\theta$	0.01 H/rad	T_2	1.814×10^{-3}
J	0.22 kg·m^2		
B	0.01 N·m/(rad/sec)		

A value of 1820 for K_{ic} gives a relatively high overshoot. So it was decided to reduce the value by half to 900. The resulting step response is shown in Fig. 4.6. It shows a small overshot of about 10% and a fast response with a rise time of about 0.2 ms. In the magnitude plot of Fig. 4.7, the magnitude starts to decay after 1500 Hz which is consistent with the target loop bandwidth design. Fig. 4.8 shows the open loop Bode plot to verify the stability. The gain margin is infinite since the phase plot does not cross 180°. The phase margin at the gain crossover frequency is about 75° which indicates a good stability.

Note that only one phase is considered so far, even though for an m phase motor there are m current loops. However, they are all identical and the final current waveforms are just different in phase shift.

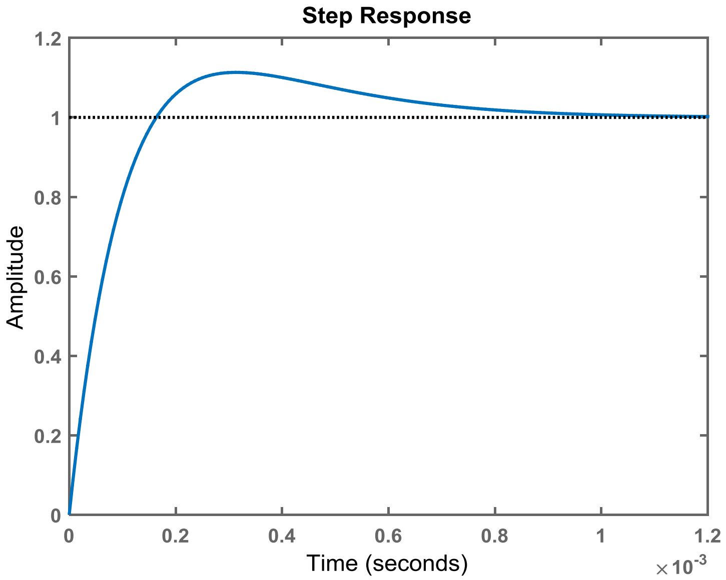

Fig. 4.6 Current loop step response

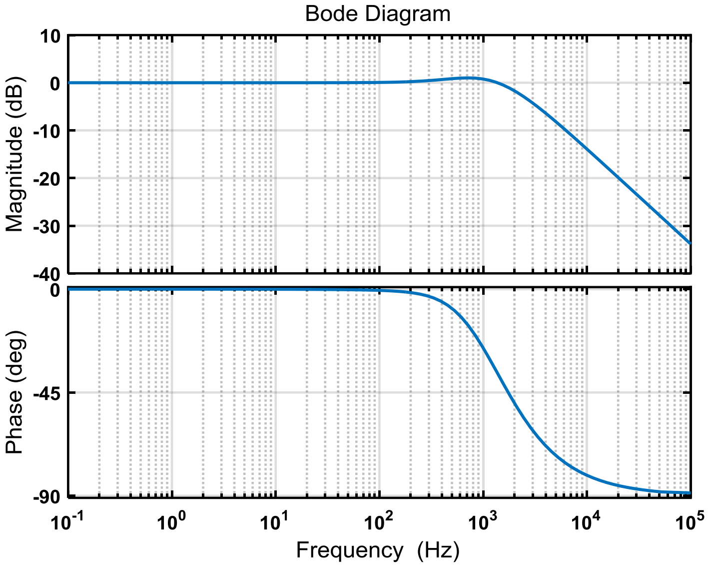

Fig. 4.7 Current loop closed-loop transfer function Bode plot

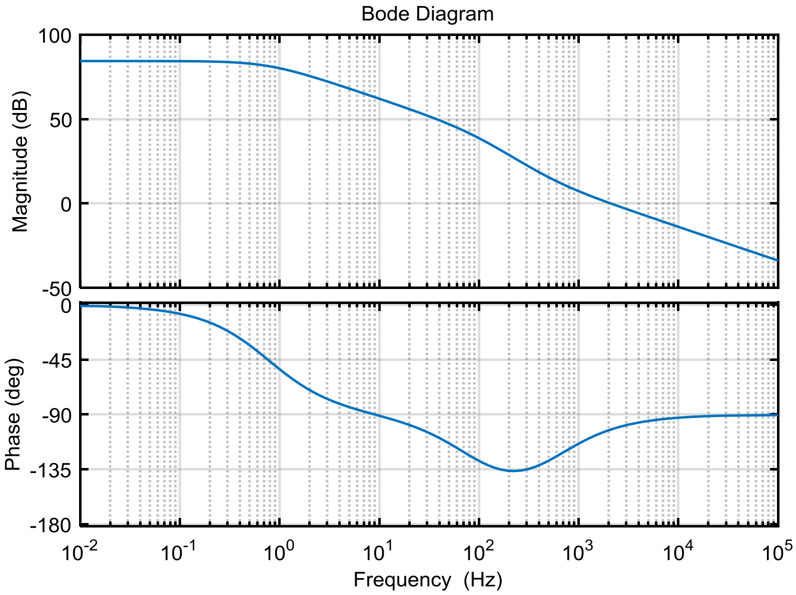

Fig. 4.8 Current loop open-loop transfer function Bode plot

4.3 Design of Speed Controller

Because the response of the current loop is usually much faster than the speed loop, the current loop delay can be neglected to simply the problem. Therefore in the speed loop, the current loop gain is approximated as unity. The speed loop block diagram is shown in Fig. 4.9. In the block diagram $K_i = 1$ and it is a second order system.

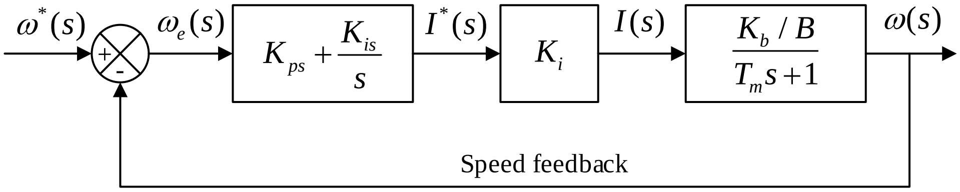

Fig. 4.9 Speed loop block diagram

The closed loop transfer function is

$$\frac{\omega(s)}{\omega^*(s)} = \frac{K_b(sK_{ps} + K_{is})}{s(T_m s + 1)B + K_b(sK_{ps} + K_{is})}$$
$$= \frac{K_{ps}K_b s + K_{is}K_b}{T_m B(s^2 + \frac{K_{ps}K_b + b}{T_m B} s + \frac{K_b K_i}{T_m B})} \tag{4.27}$$

Similar to the current controller design, the natural frequency ω_n and damping ratio ζ are given by

$$2\zeta\omega_n = \frac{K_{ps}K_b + b}{T_m B} \tag{4.28}$$

$$\omega_n^2 = \frac{K_b K_i}{T_m B} \tag{4.29}$$

Thus the K_{ps} and K_{is} can be calculated with

$$K_{ps} = \frac{2\zeta\omega_n T_m B - B}{K_b} \tag{4.30}$$

$$K_{is} = \frac{\omega_n^2 T_m B}{K_b} \tag{4.31}$$

Given $\zeta = 0.707$ and $\omega_n = 20$ Hz, the calculated results are

$$K_{pc} = 46$$

$$K_{ic} = 4000$$

Fig. 4.10 shows the speed loop step response. It also can be seen that the speed loop response is slower than the current loop, so approximating the current loop as unity gain is reasonable. The closed loop transfer function Bode plot is shown in Fig. 4.11. Fig. 4.12 shows the open loop transfer function Bode plot and at the crossover frequency of about 200 Hz, the phase margin is 65°. So the system is stable.

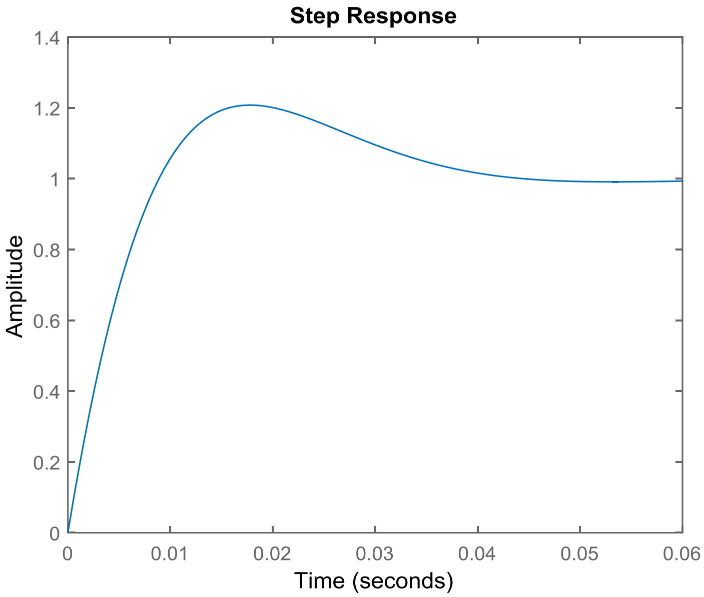

Fig. 4.10 Speed loop step response

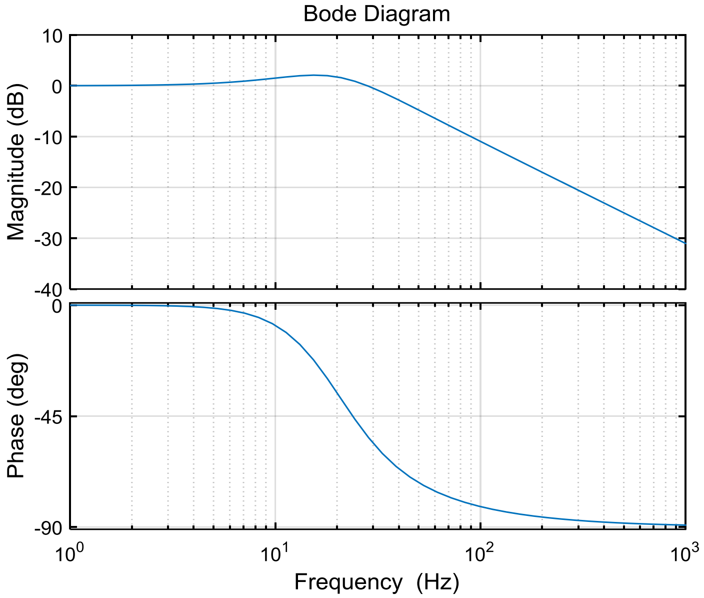

Fig. 4.11 Speed loop closed loop transfer function Bode plot

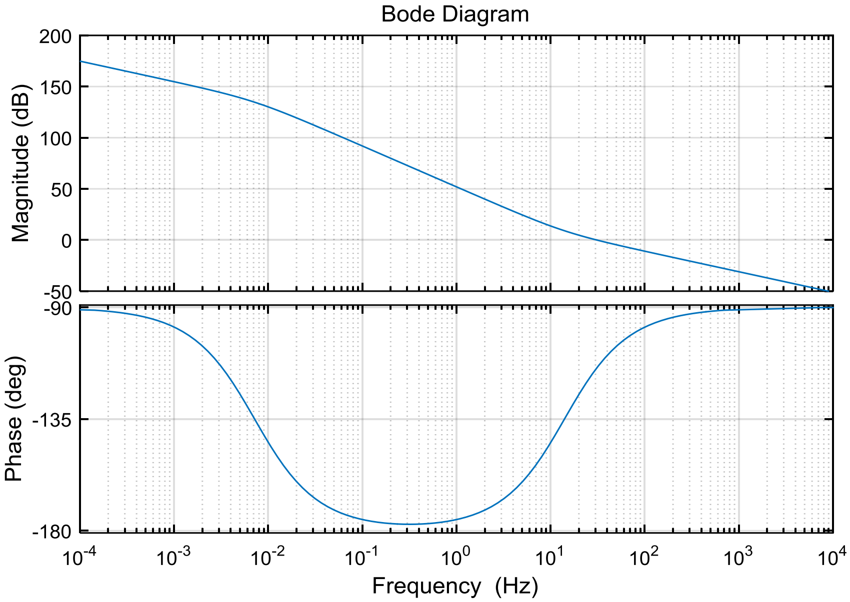

Fig. 4.12 Speed loop open loop transfer function Bode plot

5 SIMULATION AND EXPERIMENT

A Matlab/Simulink model is built based on the preceding theoretical analysis of the SRM and design of its control loops. The method of determining proper turn-on and turn-off angles to obtain the minimum torque ripple is proposed and verified. Then the mechanical design of a testbed is done with SolidWorks. The Texas Instruments DSP TMS320F28335 is used as the controller in the experimental setup to implement the proposed method for determining the firing angles in real time. Due to the current restrictions of the experimental devices, rated current cannot be achieved and the actual current is limited under 30 A.

5.1 Matlab/Simulink Simulations

The simulation model is shown in Fig. 5.1. It mainly consists of the four-phase converter, SRM model and a position estimator.

In the converter block, there are four identical converters, one for each phase. The inputs to each converter are the DC bus voltage and reference speed, while the output from each converter is the PWM voltage applied to the motor phase. Both the speed control loop and the current control loop are modeled in the converter block. In the SRM block, the motor model is built as shown in Fig. 5.2. The MATLAB Function block implements the voltage equation and inductance model described in (2.7) and section 3.3. The torque is modeled as a function of current and position using a look-up table containing data that was extracted from Maxwell FEA simulations. A variety of motor performance parameters can be obtained from the SRM block, such as current, inductance, torque, speed, etc.

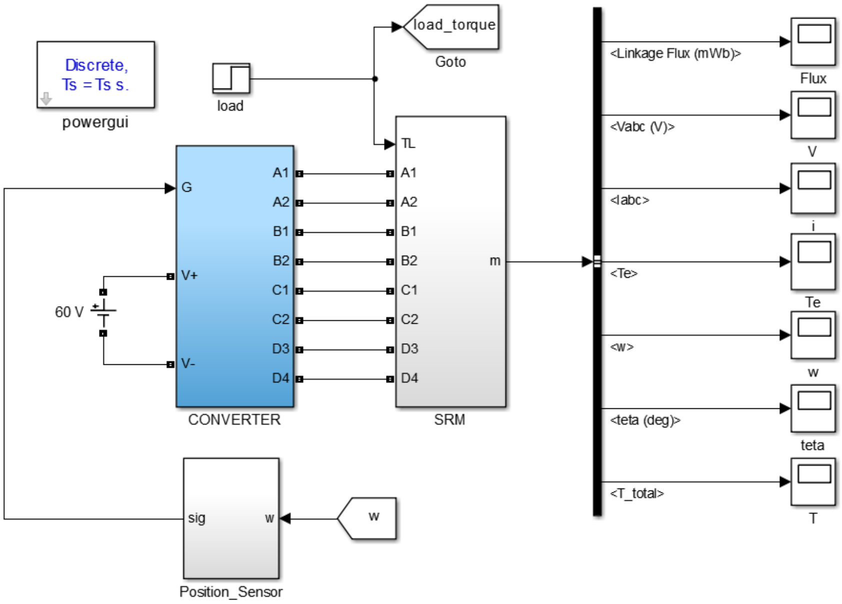

Fig. 5.1 SRM simulation model

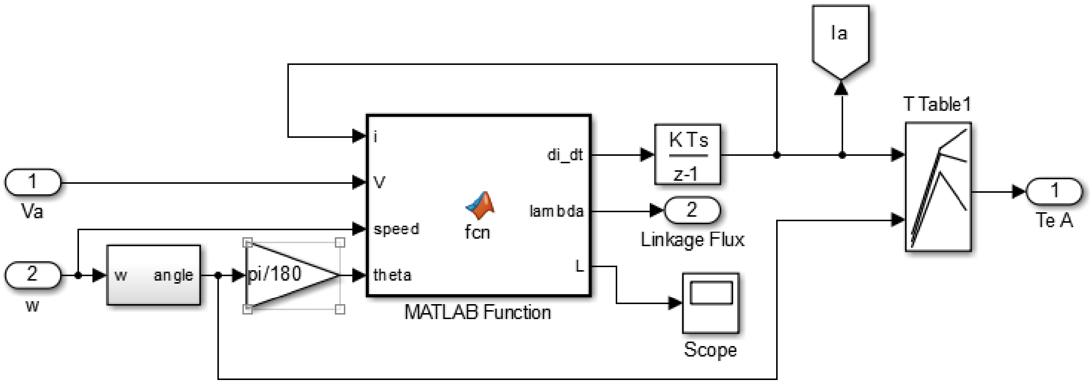

Fig. 5.2 SRM motor phase model

The position information for each phase is calculated in the position estimation block. The desired state of the phase (inactive or active) is determined by comparing the position with the turn-on and turn-off angles. If the phase is active, then the current controller will generate switching signals to regulate the phase current. Otherwise, the relevant switches will be turned off and the effect of the current controller is bypassed.

5.1.1 Basic Operation

The 200 rpm 2.8 Nm condition is simulated to illustrate the SRM operation performance and results are shown in Fig. 5.3. From top to bottom, results are current in Amps, flux linkage in mWb, speed in rpm, torque in Nm and total torque in Nm. Except for the speed and total torque, each of the other three sub-figures shows four phase variables. Current is regulated to a flat-top profile and correspondingly the flux linkage is linearly increasing. This is because current and flux are related by the inductance which has an almost linear positive slope when the phase is conducting. From the current sub-figure, it can also be seen that the phases conduct sequentially. The torque and total torque sub-figures show that there is a torque ripple at each phase commutation instance. Due to this torque ripple, the speed also experiences a slight fluctuation. However, because of the speed controller and motor inertia, this change is very small. The motor inertia serves as a low pass filter between torque and speed.

To further demonstrates the speed control and stability, the speed response to a load torque change is shown in Fig. 5.4. At time 1.5 sec, torque steps from 0.5 Nm to 2.8 Nm. It can be observed that the speed oscillates but quickly returns to the reference speed of 200 rpm. The oscillation before 0.8 sec is because of the transition from transient to steady state. Fig. 5.5 shows the current and output torque waveforms corresponding to the load torque change.

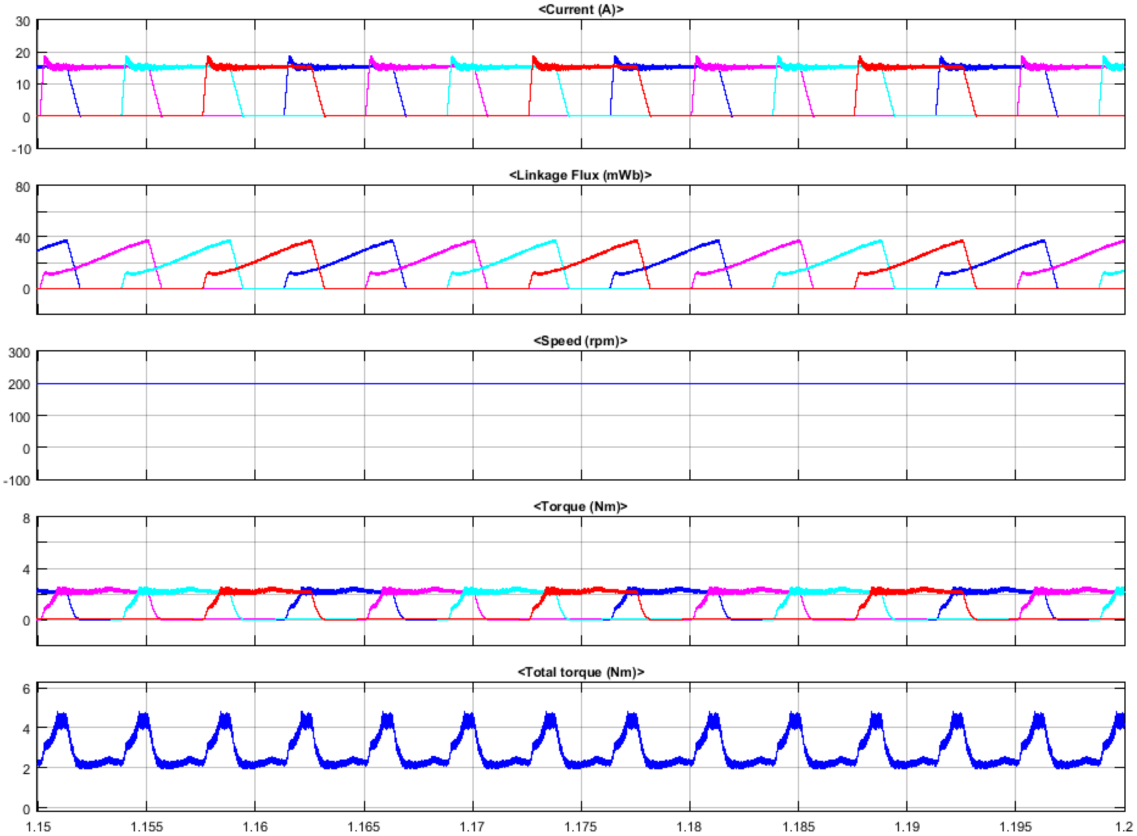

Fig. 5.3 Steady state simulation results

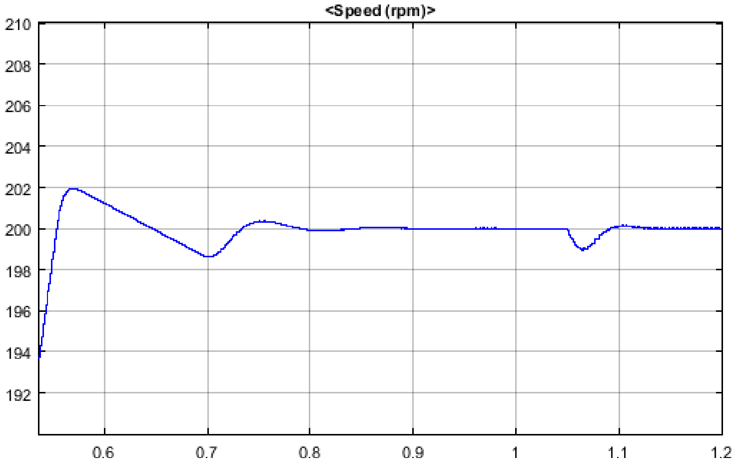

Fig. 5.4 Speed response during torque change

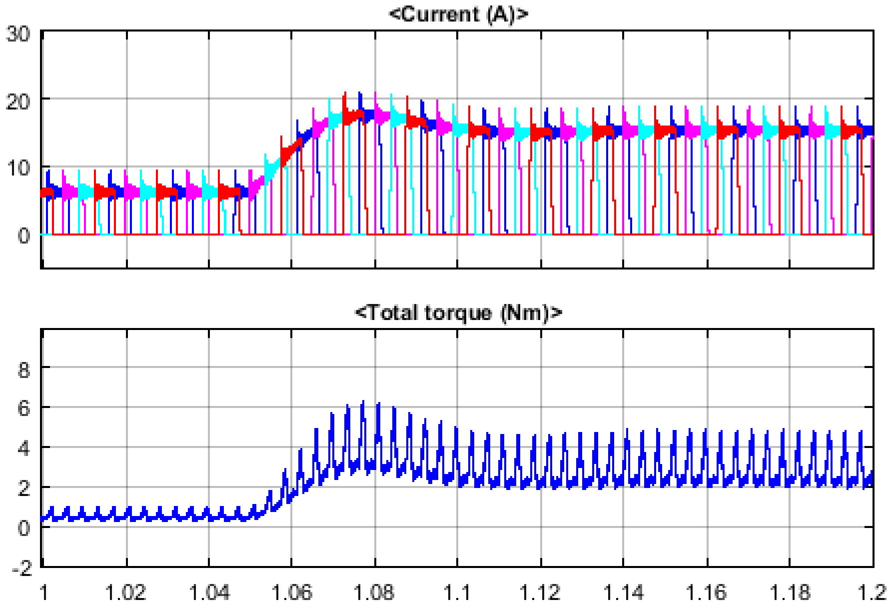

Fig. 5.5 Current and torque profiles during torque change

5.1.2 Torque Ripple Minimization

As illustrated in the torque profiles in Fig. 5.3, the total torque suffers from torque ripple because of torque overlap between different phases. If the overlap region between two phases are not properly controlled, their summation will result in the ripple. This indicates the necessity of determining the best turn-on and turn-off angles under different operation conditions.

θ_{on} is usually chosen around the unaligned position since inductance is small and current can rise quickly. A common value for θ_{on} is 0°, denoting the exactly unaligned position. However, this is not necessarily the best choice because the torque rise is not synchronized to the current rise. When current reaches the reference value, the inductance has not entered the positive slop region so torque will continue to increase gradually until the required value. In this case torque takes longer than current to rise. In order to have the current and torque to increase at the same time, θ_{on} is chosen in the way that current reaches the reference at θ_1 shown in Fig. 2.3. θ_1 indicates the inductance transition point from the unaligned region to the positive slope region. In an actual motor, θ_1 is not as evident as it is in the idealized profile in Fig. 2.3. For the motor studied in this thesis, θ_1 is approximated as 1.25°. Since the phase resistance is small and the unaligned inductance is almost constant, (2.7) reduces to the inductor voltage-current relation. Thus the rise time t_r can be calculated by

$$t_r = \frac{L_u \cdot I_{ref}}{V_{dc}} \tag{5.1}$$

where $L_u = 0.63$ mH is the inductance at the unaligned position and I_{ref} is the reference current at a certain operation point. Clearly at a given speed, a certain angular distance will be traversed during t_r. Subtracting this angle from θ_1 will give the turn-on angle satisfying the aforementioned criterion. In short, θ_{on} is given by

$$\theta_{on} = \theta_1 - \frac{360 \cdot \omega}{60} \cdot t_r \tag{5.2}$$

where ω is the motor speed in rpm.

The next thing is to determine the best value of θ_{off} for reducing torque ripple. According to (2.3), the stroke angle for this motor is 4.5°. The difference between θ_{on} and θ_{off} should be at least the stroke angle θ_{sk} to prevent a reduction of the average torque. With θ_{off} greater than $\theta_{on} + \theta_{sk}$ there will be more torque overlap. In order to determine the best turn-off angle, θ_{off} is varied within a small range at different operating points which are specified by reference speed and load torque. For a given operating point, θ_{off} is varied with a step of 0.25° and the standard deviation of the output torque at steady state is calculated as the indication of torque ripple. The value of θ_{off} corresponding to the smallest torque standard deviation is selected as the best turn-off angle. Table 5.1 shows the calculated turn-on angles. The row index is torque in Nm and the column index is speed in rpm. As the speed and/or load torque increases, the turn-on angle decreases, meaning it gets closer to the exactly unaligned position.

Table 5.1 Turn-on angles at different operation points

	50	100	150	200	250	300	350	400	450	500	560
0.5	1.228	1.206	1.183	1.161	1.139	1.117	1.095	1.073	1.050	1.028	1.002
1	1.217	1.184	1.151	1.118	1.085	1.052	1.019	0.986	0.953	0.920	0.881
1.5	1.210	1.170	1.130	1.091	1.051	1.011	0.971	0.931	0.891	0.851	0.804
2	1.203	1.156	1.110	1.063	1.016	0.969	0.923	0.876	0.829	0.782	0.726
2.5	1.198	1.146	1.094	1.042	0.990	0.938	0.886	0.834	0.782	0.730	0.667
3	1.193	1.136	1.079	1.022	0.965	0.908	0.851	0.794	0.737	0.680	0.612
3.5	1.188	1.126	1.064	1.002	0.940	0.878	0.817	0.755	0.693	0.631	0.556
4	1.184	1.118	1.051	0.985	0.919	0.853	0.786	0.720	0.654	0.588	0.508
4.5	1.180	1.110	1.040	0.970	0.900	0.830	0.760	0.690	0.620	0.550	0.465
5	1.176	1.102	1.028	0.954	0.881	0.807	0.733	0.659	0.585	0.511	0.423
5.5	1.172	1.095	1.017	0.939	0.861	0.784	0.706	0.628	0.551	0.473	0.380

The 200 rpm 2.8 Nm case is simulated again with $\theta_{on} = 1.03°$ and $\theta_{off} = 5.53°$. From top to bottom Fig. 5.6 shows the resulting phase current, torque and total torque.

Comparing the phase current and torque, it can be seen that they increase during the same time intervals so the torque rise is indirectly controlled by controlling the current. In addition, compared to the total torque in Fig. 5.3, the torque ripple is also reduced.

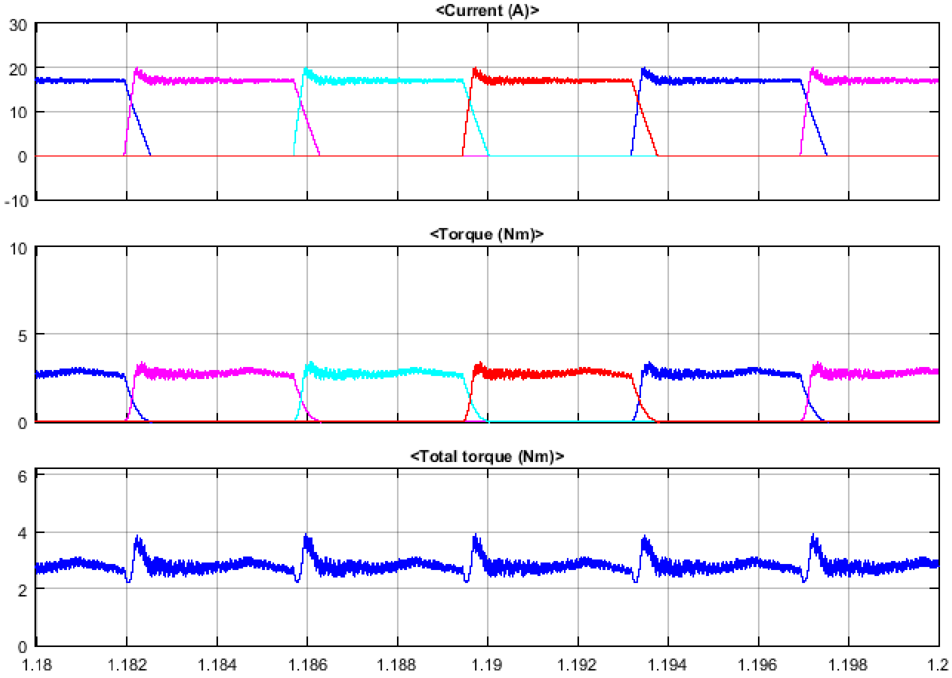

Fig. 5.6 Simulation results with optimized firing angles at 200 rpm 2.8 Nm

5.2 Experiment

The experimental setup consists of a testbed on which the SRM and a DC generator sit, a SEMIKRON IGBT-based converter, and a TI TMS320F28335 DSP which serves as the control core. The DC generator is driven by the ABB DCS800 drive to load the SRM. An encoder with 4096 pulses per revolution is used to obtain the motor position. Four-phase currents are sensed for current control.

5.2.1 Experimental Setup

The DC motor was originally mounted on the GE motor-generator testbed. To fit the SRM with this testbed and connect with the DC motor, another Aluminum base was designed in SolidWorks.

Since the SRM has an outer rotor structure and its shaft is stationary, an extra custom designed end cap is required to transmit the torque to a rotatory shaft so that it can be coupled with the load motor. Fig. 5.7 shows the assembly of the SRM and the end cap. The name of each part is listed in Table 5.2. The end cap is made up of two parts, one is the collar and the other is the extended shaft. The collar is attached to the SRM rotor. The SRM shaft goes inside the end cap, contacting the inner surface of the end cap through a bearing. The cap's extended shaft is used to mount the encoder and connect to the load machine via the coupling. In this way, the outer rotor transfers electromagnetic torque through the extended shaft to the load. The actual testbed is shown in Fig. 5.8.

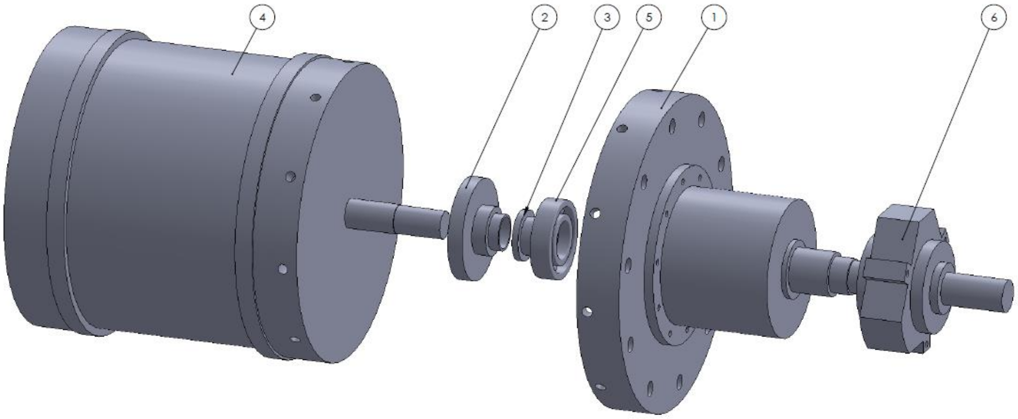

Fig. 5.7 SRM and end cap assembly

Table 5.2 List of parts of SRM and end cap assembly

Item No.	Item Name	Function
1	End cap	Transmit torque to the rotatory shaft
2	Cap locator	Keep the end cap and SRM rotor concentric
3	Shaft sleeve	Fit the SRM shaft with bearing
4	SRM	Motor under test
5	Bearing	Connect the SRM stationary shaft and rotatory end cap
6	Encoder	Measure motor position

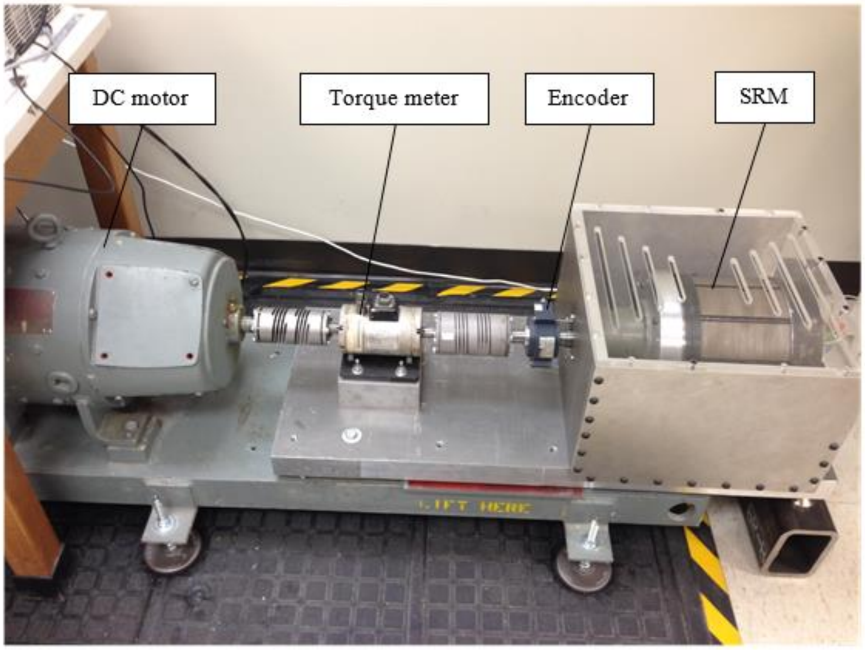

Fig. 5.8 Motor testbed

Fig. 5.9 shows the control circuit. It consists of a DSP, an interface board and converters. The figure only shows the converter box for one phase. The interface board senses currents and connects the DSP and converters. The sensed currents are fed into the ADC channels on the DSP.

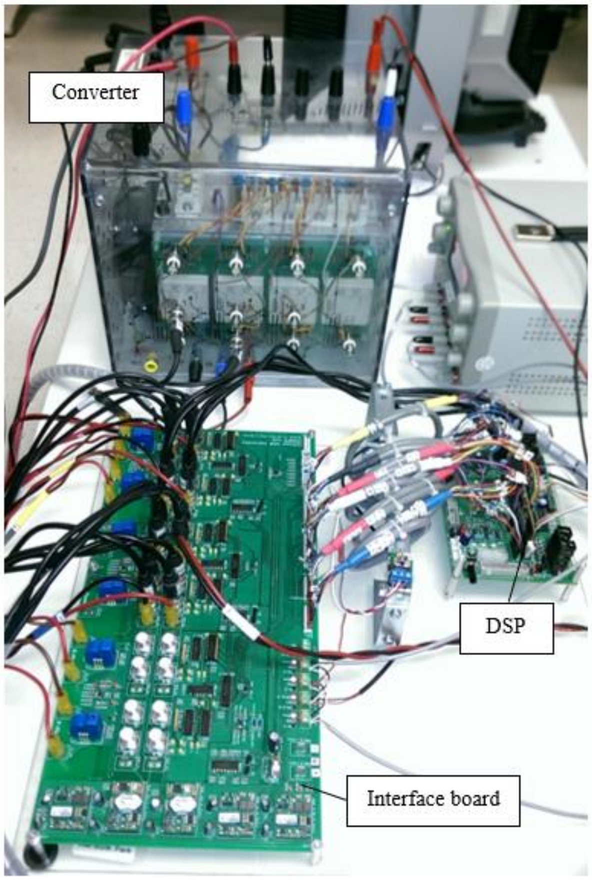

Fig. 5.9 Control hardware

5.2.2 Experimental Results

Fig. 5.10 shows the experimental setup block diagram. The dashed rectangular box indicates the DSP and the functions that it implements. The motor position and phase currents are fed into the DSP. The main modules and functions of the DSP are briefly described below.

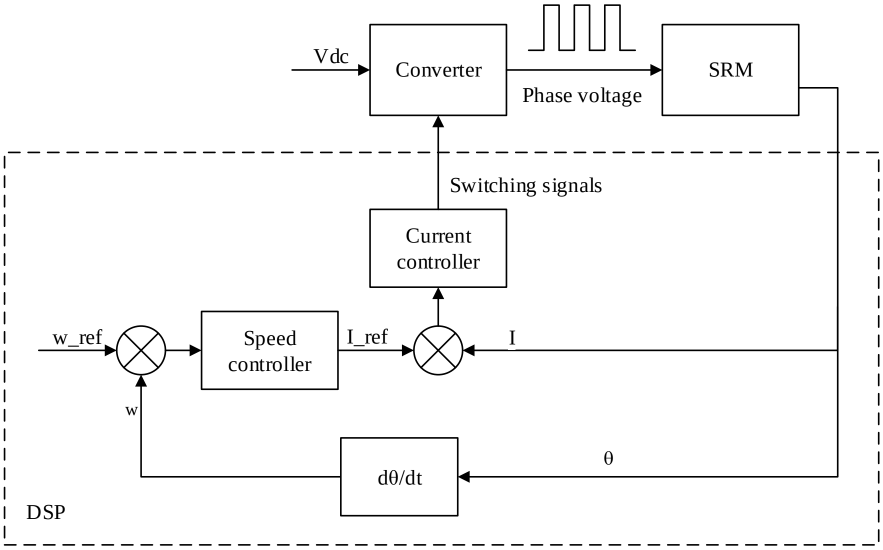

Fig. 5.10 Block diagram of experimental setup

- Position and speed measurement. Uses the Quadrature Encoder Pulse (QEP) circuit in the DSP and the shaft encoder to determine the rotor position. Speed is calculated based on an interrupt.
- Speed controller. A PI controller processes the speed error and outputs the reference current.
- Current measurement. 4 ADC channels are used to measure phase currents through a current sensing circuit. The average of 16 samples is used to filter noise and produce one valid current sample value. The current is sampled at an effective rate of 15 kHz.
- Current controller. The current error is processed by a PI controller which sends compare values to the PWM peripheral in DSP. Then the switch signals are generated and output to the converters.

- Commutation module. This module adjusts the firing angles at different operating conditions, based on the torque ripple.

Fig. 5.11 shows the current, voltage, top switch and bottom switch signals of one phase, labeled as 1-4 respectively. During the conduction period, the top switch is turned on and off while the bottom switch is always on. The voltage on the phase is either the positive DC bus voltage or 0. During the phase is turned off, both switches are off and the phase voltage becomes the negative DC bus voltage.

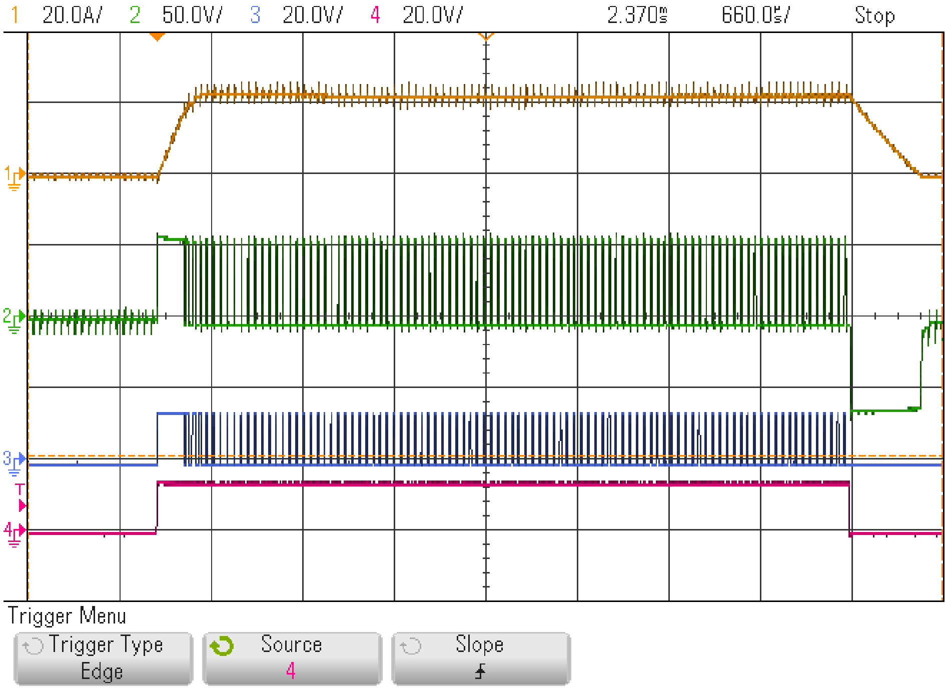

Trigger Type Edge
Source 4
Slope

Fig. 5.11 Current, voltage and switching signals

The same firing-angle optimization algorithm used in the simulations was implemented in the DSP. θ_{on} is first calculated based on the actual speed and current. Then θ_{off} is varied to test the torque performance. At each value of θ_{off}, the instantaneous torque is estimated according to current and position. 5000 torque values are sampled to calculate the torque ripple. To save calculation time in the DSP, instead of using standard deviation, torque ripple ΔT is defined as

$$\Delta T = \sum_{i=0}^{N} |T_i - T_{avg}| \tag{5.3}$$

where N is the number of torque samples, T_i is the ith torque sample and T_{avg} is the average torque.

The 200 rpm 2.8 Nm condition was tested to verify the proposed method. Fig. 5.12 shows the estimated output torque when $\theta_{on} = 0.5°$ and $\theta_{off} = 6.5°$ (case 1). As a comparison, the torque with optimized firing angles $\theta_{on} = 1.02°$ and $\theta_{off} = 5.52°$ (case 2) is shown in Fig. 5.13. The firing angles were calculated and tuned in the code with the proposed method. The estimated torque in these two figures is in good agreement with the simulation results in Fig. 5.3 and Fig. 5.6. According to (5.3), the torque ripple is 5280 Nm and 1038 Nm, respectively. It can be seen in Fig. 5.13, that the magnitude of the torque ripple is smaller and the durations of the torque spikes are shorter. Thus, optimizing the firing angles does in fact reduce the torque ripple.

Spectrum analysis is applied to the torque signal from the torque meter. It can be analyzed that the torque ripple is a result of the phase commutation. Each time two phases commutate, it results in a torque ripple. Thus the fundamental frequency *f* of torque ripple can be estimated by (5.4) as below

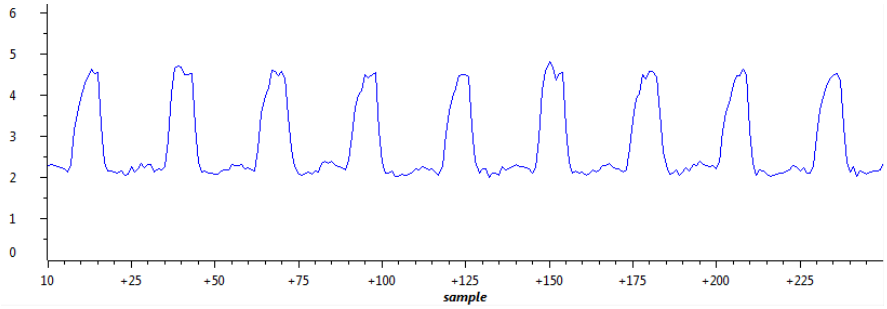

Fig. 5.12 Estimated output torque without optimized firing angles

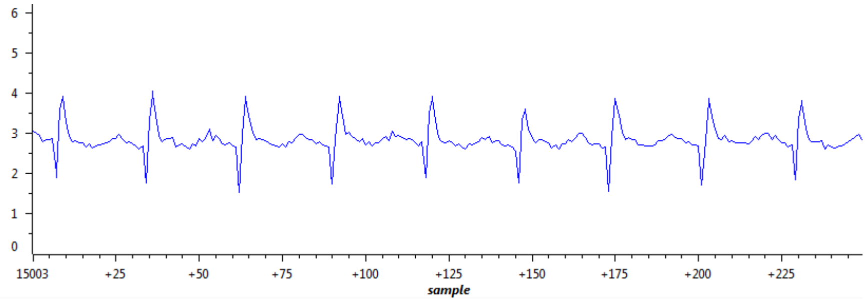

Fig. 5.13 Estimated output torque with optimized firing angles

$$f = \frac{\omega}{60} * m * N_r \tag{5.4}$$

where ω is the motor speed in rpm. When speed is 200 rpm, the torque ripple frequency is about 267 Hz. Fig. 5.14 shows the magnitude of the fundamental frequency component of the torque signals from the spectrum analyzer screen. (a) is for non-optimized case 1 and (b) is for optimized case 2. At around 268 Hz, the magnitude of case 2 is smaller than case 1. Fig. 5.15 shows the average value of the torque signals. (a) is the non-optimized case and it shows at 0 Hz the value is about 196.1 mV. (b) is the optimized case and the value is about 197.4 mV. The data shown in (c) was exported from the spectrum analyzer and then plotted in Matlab in higher quality. This indicates that for the optimized firing angles, the torque ripple is smaller and the average torque remains same. Thus, it can be claimed the normalized torque ripple is indeed reduced.

(a) (b)

Fig. 5.14 Magnitude of the output torque fundamental frequency component

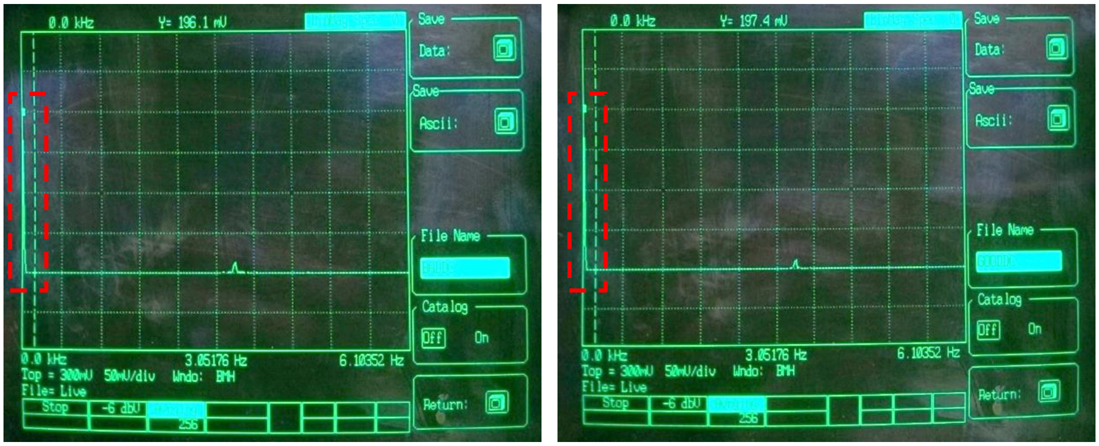

(a) (b)

Fig. 5.15 Magnitude of the output torque DC component

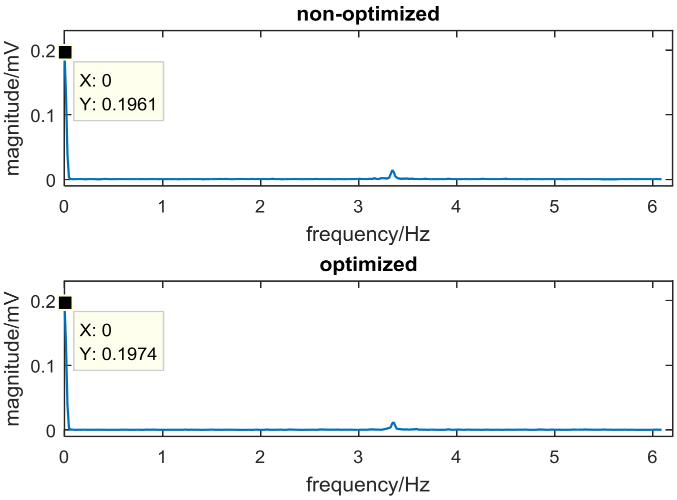

(c)

Fig. 5.15 Continued

To further verify the method, another condition – 330 rpm and 2.8 Nm load torque – was tested. The fundamental frequency of torque ripple is estimated as 440 Hz by (5.4). The firing angles for non-optimized case are the same as before, 0.5° and 6.5°. The optimized turn-on and turn-off angle, under this speed, are determined to be 0.87° and 5.37° respectively. Fig. 5.16 shows the spectrum analysis results. Similar to before, the magnitude of the fundamental frequency component of the optimized case, shown in (b), is smaller than that of the non-optimized one, which is shown in (a).

(a) (b)

Fig. 5.16 Magnitude of the output torque fundamental frequency component at 330 rpm

6 SUMMARY AND FUTURE WORK

This thesis proposes an on-line self-tuning algorithm for SRMs to find the best firing angles at different operating conditions in real time. The method combines both analysis-based calculation and trial and error. At an arbitrary working point, the algorithm can find the best turn-on and turn-off angles so that the torque ripple is minimized. The system transfer functions are carefully derived and used to design the dual-loop control. The SRM is first simulated in Matlab/Simulink to verify the basic operation and torque ripple minimization. Then the performance is experimentally verified in a custom designed testbed. Spectrum analysis of the output torque is used to prove that optimizing the firing angles reduces the normalized torque ripple.

The following ideas can be researched for future work.

1. Estimate the current drop time.

In the section 5.1.2, the current rise time is studied and the turn-on angle is calculated so that the current and torque rise within the same time. Similarly, the current drop time can be analyzed to see how the torque drop is related to the current drop. Then proper turn-off angle for maximum average torque purpose can be determined.

2. Direct torque control.

In the dual-loop control scheme of this thesis, the output of the speed loop serves as the current loop reference. Instead, the current loop can be replaced by a torque control loop with Torque Sharing Function (TSF). The TSF can ensure that the torque summation of two phases is smooth. This method requires a very accurate model to estimate the actual torque of each phase.

3. Indirect torque control with TSF.

A torque-current relation block along with TSF can be added between the speed loop and current loop. The reference current of each phase is determined by the reference torque and TSF. In this method, a torque-current relation model is required that can be challenging especially during saturated conditions.

REFERENCES

[1] R. Krishnan, Switched Reluctance Motor Drives: Modeling, Simulation, Analysis, Design, and Applications: CRC Press, 2001.

[2] T. J. E. Miller, Electronic Control of Switched Reluctance Machines: Newnes, 2001.

[3] K. Vijayakumar, R. Karthikeyan, S. Paramasivam, R. Arumugam, and K. N. Srinivas, “Switched Reluctance Motor Modeling, Design, Simulation, and Analysis: A Comprehensive Review,” Magnetics, IEEE Transactions on, vol. 44, pp. 4605-4617, 2008.

[4] Z. Jinhui and A. V. Radun, “A New Method to Measure the Switched Reluctance Motor's Flux,” in Applied Power Electronics Conference and Exposition, 2005. APEC 2005. Twentieth Annual IEEE, 2005, pp. 1994-1999 Vol. 3.

[5] N. H. Fuengwarodsakul, S. Bauer, O. Tsafak, and R. W. De Doncker, “Characteristic Measurement System for Automotive Class Switched Reluctance Machines,” in Power Electronics and Applications, 2005 European Conference on, 2005, pp. 10 pp.-P.10.

[6] L. Kaiyuan, P. O. Rasmussen, and A. E. Ritchie, “Investigation of Flux-Linkage Profile Measurement Methods for Switched-Reluctance Motors and Permanent-Magnet Motors,” Instrumentation and Measurement, IEEE Transactions on, vol. 58, pp. 3191-3198, 2009.

[7] R. Saxena, B. Singh, and Y. Pahariya, “Measurement of Flux Linkage and Inductance Profile of Srm,” International Journal of Computer and Electrical Engineering, vol. 2, p. 5, 2010.

[8] J. Mahdavi, G. Suresh, B. Fahimi, and M. Ehsani, “Dynamic Modeling of Nonlinear Srm Drive with Pspice,” in Industry Applications Conference, 1997. Thirty-Second IAS Annual Meeting, IAS '97., Conference Record of the 1997 IEEE, 1997, pp. 661-667 vol.1.

[9] G. Hongwei, F. R. Salmasi, and M. Ehsani, “Inductance Model-Based Sensorless Control of the Switched Reluctance Motor Drive at Low Speed,” Power Electronics, IEEE Transactions on, vol. 19, pp. 1568-1573, 2004.

[10] J. Dang, “Switched Reluctance Machine Electromagnetic Design and Optimization,” Ph.D. Dissertation, Dept. of Electrical and Computer Engineering, Georgia Institute of Technology, Atlanta, GA, 2015.

[11] M. Balaji and V. Kamaraj, “Design Optimization of Switched Reluctance Machine Using Particle Swarm Optimization,” in Electrical Energy Systems (ICEES), 2011 1st International Conference on, 2011, pp. 164-169.

[12] J. W. Jiang, B. Bilgin, B. Howey, and A. Emadi, “Design Optimization of Switched Reluctance Machine Using Genetic Algorithm,” in Electric Machines & Drives Conference (IEMDC), 2015 IEEE International, 2015, pp. 1671-1677.

[13] X. Wang, “Modeling and Implementation of Controller for Switched Reluctance Motor with Ac Small Signal Model,” M.S. Thesis, Dept. of Electrical Engineering, Virginia Polytechnic Institute and State University, Blacksburg, VT, 2001.

[14] S. K. Sahoo, S. K. Panda, and X. Jian-Xin, “Indirect Torque Control of Switched Reluctance Motors Using Iterative Learning Control,” IEEE Transactions on Power Electronics, vol. 20, pp. 200-208, 2005.

[15] P. V. N. P. P.Srinivas, “Pwm Control of Asymmetrical Converter Fed Switched Reluctance Motor Drive ”, 2015.

[16] B. Blanque, J. I. Perat, P. Andrada, and M. Torrent, “Improving Efficiency in Switched Reluctance Motor Drives with Online Control of Turn-on and Turn-Off Angles,” in Power Electronics and Applications, 2005 European Conference on, 2005, pp. 9 pp.-P.9.

[17] J. Ye, “Advanced Control Methods for Torque Ripple Reduction and Performance Improvement in Switched Reluctance Motor Drives,” Ph.D. Dissertation, Dept. of Electrical and Computer Engineering, McMaster University, Hamilton, Canada, 2014.

[18] H.-K. Bae, “Control of Switched Reluctance Motors Considering Mutual Inductance,” 2000.

[19] K. M. Rahman, B. Fahimi, G. Suresh, A. V. Rajarathnam, and M. Ehsani, “Advantages of Switched Reluctance Motor Applications to Ev and Hev: Design and Control Issues,” Industry Applications, IEEE Transactions on, vol. 36, pp. 111-121, 2000.

[20] P. C. Desai, M. Krishnamurthy, N. Schofield, and A. Emadi, “Novel Switched Reluctance Machine Configuration with Higher Number of Rotor Poles Than Stator Poles: Concept to Implementation,” Industrial Electronics, IEEE Transactions on, vol. 57, pp. 649-659, 2010.

[21] W. Sun, Y. Li, J. Huang, and N. Zhang, “Vibration Effect and Control of in-Wheel Switched Reluctance Motor for Electric Vehicle,” Journal of Sound and Vibration, vol. 338, pp. 105-120, 3/3/ 2015.

[22] B. Bilgin, A. Emadi, and M. Krishnamurthy, “Comprehensive Evaluation of the Dynamic Performance of a 6/10 Srm for Traction Application in Phevs,” Industrial Electronics, IEEE Transactions on, vol. 60, pp. 2564-2575, 2013.

[23] B. Anvari, Y. Li, and H. Toliyat, “Comparison of Outer Rotor Permanent Magnet and Magnet-Less Generators for Direct-Drive Wind Turbine Applications,” in Electric Machines & Drives Conference (IEMDC), 2015 IEEE International, 2015, pp. 181-186.

[24] D. A. Torrey, “Switched Reluctance Generators and Their Control,” IEEE Transactions on Industrial Electronics, vol. 49, pp. 3-14, 2002.

[25] R. Cardenas, R. Pena, M. Perez, J. Clare, G. Asher, and P. Wheeler, “Control of a Switched Reluctance Generator for Variable-Speed Wind Energy Applications,” IEEE Transactions on Energy Conversion, vol. 20, pp. 781-791, 2005.

[26] R. Arumugam, J. F. Lindsay, and R. Krishnan, “Sensitivity of Pole Arc/Pole Pitch Ratio on Switched Reluctance Motor Performance,” in Industry Applications Society Annual Meeting, 1988., Conference Record of the 1988 IEEE, 1988, pp. 50-54 vol.1.

[27] B. Akin and M. Bhardwaj, “Trapezoidal Control of Bldc Motors Using Hall Effect Sensors,” Texas Instruments, Application Note SPRABQ6, July 2013.

[28] M. T. DiRenzo, “Switched Reluctance Motor Control–Basic Operation and Example Using the TMS320F240,” Texas Instruments, Application Report SPRA420A, Feb. 2000.

[29] T. A. Lipo, Introduction to Ac Machine Design: Wisconsin Power Electronics Research Center, University of Wisconsin, 2004.

[30] B. Fahimi, “Control of Vibration in Switched Reluctance Motor Drives,” Ph.D Dissertation, Dept. of Electrical and Computer Engineering, Texas A&M University, College Station, TX, 1999.

[31] R. W. Erickson and D. Maksimovic, Fundamentals of Power Electronics: Springer Science & Business Media, 2007.

[32] M. Driels, Linear Control Systems Engineering: McGraw-Hill Higher Education, 1995.